



# Semiempirical Models of the Solar Atmosphere. I. The Quiet- and Active Sun Photosphere at Moderate Resolution

J.M. Fontenla, E. Avrett, Gérard Thuillier, J. Harder

## ► To cite this version:

J.M. Fontenla, E. Avrett, Gérard Thuillier, J. Harder. Semiempirical Models of the Solar Atmosphere. I. The Quiet- and Active Sun Photosphere at Moderate Resolution. *The Astrophysical Journal*, 2006, 639, pp.441-458. 10.1086/499345 . hal-00068916

**HAL Id: hal-00068916**

**<https://hal.science/hal-00068916>**

Submitted on 19 Jul 2020

**HAL** is a multi-disciplinary open access archive for the deposit and dissemination of scientific research documents, whether they are published or not. The documents may come from teaching and research institutions in France or abroad, or from public or private research centers.

L'archive ouverte pluridisciplinaire **HAL**, est destinée au dépôt et à la diffusion de documents scientifiques de niveau recherche, publiés ou non, émanant des établissements d'enseignement et de recherche français ou étrangers, des laboratoires publics ou privés.

# SEMIEMPIRICAL MODELS OF THE SOLAR ATMOSPHERE. I. THE QUIET- AND ACTIVE SUN PHOTOSPHERE AT MODERATE RESOLUTION

J. M. FONTENLA,<sup>1</sup> E. AVRETT,<sup>2</sup> G. THUILLIER,<sup>3</sup> AND J. HARDER<sup>1</sup>

*Received 2005 June 4; accepted 2005 October 24*

## ABSTRACT

In this paper we study and modify previous semiempirical models of the solar photosphere as observed at moderate spatial and temporal resolution ( $\sim 3''$  and  $\sim 30$  minutes, respectively) in the main quiet- and active Sun component features. Our present models are constructed to match the relevant available observations at this resolution for which a one-dimensional and time-independent stratification is reasonable. The models do not describe the fine structure and temporal variability observed in high-resolution images but correspond to a “radiation averaging” over the fine-structure and  $p$ -mode variations. We use the observed limb darkening in the range  $0.3\text{--}2.4\ \mu\text{m}$ , as well as the absolute intensities and details of the spectral continua and lines in this range, to validate and adjust the models. Using the method described in a previous paper, we compute the emergent radiation from our models in full detail for the visible and IR continuum and the lines in the interval  $0.3\text{--}5\ \mu\text{m}$  for which we have atomic data from NIST ( $\sim 13,000$  lines used) and molecular data from HITRAN and Gray & Corbally ( $\sim 480,000$  molecular lines used). The observations, abundances, and atomic/molecular data are improved over previous work and yield models that better fit the observations. In addition, we construct a new penumbra model. The visible and IR detailed spectra computed from these models provide insight for understanding the effects of magnetic fields on the solar irradiance and are useful tools for computing synthetic spectral irradiances in different solar activity configurations.

*Subject headings:* Sun: activity — Sun: atmosphere

*Online material:* machine-readable tables

## 1. INTRODUCTION

We construct new semiempirical models of the quiet- and active Sun components of the photosphere in order to improve our understanding of the effect on the spectra of various physical processes considered in our models of the solar atmosphere and to improve the parameters in these models that correspond to spatial and temporal resolution of  $\sim 3''$  and  $\sim 30$  minutes, respectively. Our models are based on solving equations that describe the structure and the detailed transport of radiation through our model atmosphere consistently with the observed spectra at the moderate spatial and temporal resolution we consider. The models provide the distribution of temperature, density, and other physical parameters characterizing the one-dimensional model that provides the best fit to the observed spectra. Since our knowledge of some of the physical processes is incomplete, it is necessary to use ad hoc parameters, e.g., to describe the effects of turbulence. In constructing these models we attempt to maintain physical consistency to the extent possible, even though the underlying fine structure is not explicitly accounted for and some processes are not fully understood, e.g., magnetic heating.

This approach contrasts with, but does not oppose, the purely theoretical modeling of physical processes in which the distribution of temperature and density are computed from first principles and from initial and boundary conditions, e.g., numerical simulations of magneto-convection. The primary goal of theoretical modeling is to understand basic physical processes by a fully consistent treatment, and secondarily to match the ob-

servations in detail, given the simplifications made. Both approaches are important for making progress in our understanding of the solar atmosphere.

In the present paper we consider semiempirical models of the solar photosphere at spatial resolution of a few arcseconds and temporally averaged over several  $p$ -mode oscillation periods. At this resolution, the granulation and other fine structures are not resolved, and only “radiation-effective” physical parameters can be derived that correspond to an averaging over the fine structure. This averaging is weighted by its effects on the observed emergent radiation. Our photospheric models are derived from the observed visible and infrared (IR) continuum and from photospheric line radiation.

An issue that affects any type of model is the assumed dimensionality. One-dimensional models are a good approximation when the horizontal scale is much larger than the vertical scale of the resolution elements under consideration. In this case the gradients and fluxes are predominantly vertical. The one-dimensional approach is used in the present models because the horizontal resolution scale we consider is much larger than the gravitational height scale and also much larger than the overall vertical extent of the photosphere. Therefore, the density and temperature variations and the photon flux are mostly vertical except at the boundaries of the resolution elements. However, as we show in the case of the penumbra observations, some relatively minor departures from one-dimensionality have small but measurable effects on the emitted penumbral radiation.

In § 2 we discuss the implications of high-resolution observations and time-dependent simulations on the interpretation of the medium-resolution models we consider. As more complete higher resolution spectral observations become available, it would be useful to apply our semiempirical analysis to those data as well. (However, at very high resolution, three-dimensional modeling would be necessary, since, for example, the width of intergranular

<sup>1</sup> Laboratory for Atmospheric and Space Physics, University of Colorado, Boulder, CO 80309; fontenla@lasp.colorado.edu.

<sup>2</sup> Harvard-Smithsonian Center for Astrophysics, 60 Garden Street, Cambridge, MA 02138.

<sup>3</sup> Service d’Aéronomie du Centre National de la Recherche Scientifique, Bp3, F91371 Verrières-le-Buisson, France.

lanes is comparable with the height scale.) In some cases it may not be practical to produce semiempirical models at too high a resolution, and statistical approaches based on distribution functions may be more convenient.

The quiet-Sun chromospheric/photospheric model C given by Vernazza et al. (1981, hereafter VAL81) was modified by Avrett (1985), increasing the temperature minimum, and by Maltby et al. (1986), adjusting the photosphere to improve agreement with the Neckel & Labs (1984) visible data and the Pierce (1954) IR continuum data. Fontenla et al. (1990, 1991, 1993, 2002, hereafter FAL90, FAL91, FAL93, and FAL02, respectively) carried out theoretical modeling of the transition region energy balance at the footpoints of coronal loops, taking into account H and He particle diffusion and mass flows. These papers used the photospheric and chromospheric parts of the reference model of Maltby et al. (1986) and modified versions of VAL81 models A and F to determine the boundary conditions for the transition region modeling. FAL93 included a complete listing of models A, C, and F but with the previous transition region replaced by the energy balance distribution. The FAL93 paper also includes a full listing of a faculae model P based on a model by Lemaire et al. (1981).

Most of the models presented here are based on those by Fontenla et al. (1999), which introduced small modifications to the models listed by FAL93 and added several models: model E for the network based on modifications of the corresponding VAL81 model, model H for plage, and a sunspot umbra model similar to the model M by Maltby et al. (1986), all with energy balance transition regions.

In the present paper we study in detail the Fontenla et al. (1999) models and significantly modify them (except model C) to account for recent observations, and we add an additional model devised for sunspot penumbrae, model R, again based on moderate-resolution data. We compute in detail the emitted visible and IR continuum and line spectra produced by the models at several disk positions, as well as the irradiance spectrum, using an updated version of the computations described by Fontenla et al. (1999) and the latest published elemental abundance values.

As is usual in photospheric modeling (e.g., Gingerich & de Jager 1968; Gingerich et al. 1971), we adjust the temperature stratification as a function of gas pressure in such a way that the computed intensities match the observed disk center intensities and center-to-limb variation (CLV) at various wavelengths. We base this study on our CLV observations using the Precision Solar Photometric Telescope (PSPT, e.g., Vogler et al. 2005)<sup>4</sup> operated at Mauna Loa Solar Observatory by the High Altitude Observatory, especially in the red band, and on other data shown by Pierce (2000) and Solanki (2000) from references therein. For magnetic features models we examine the contrast with respect to the cell center model C at several wavelengths, as given by  $C_{\text{model}} = [(I_{\text{model}}/I_C) - 1]$ , where  $I_{\text{model}}$  is the emergent intensity for a certain model and position on the disk and  $I_C$  is the intensity for model C at the same position on the disk. For our analysis we consider many wavelengths, but for simplicity we show in detail here only the CLV of the model C intensity and active features models contrast at two wavelengths, one representative of the continuum from the top photospheric layers (606 nm) and the other of the deepest observable photospheric layers (1600 nm). We also compare the computed absolute flux for model C as a function of wavelength with recent solar irradiance observations for studying the temperature values on an absolute scale, and we consider profiles of some well-known photospheric lines, mostly

for verification purposes and diagnosis of the microturbulent broadening velocity.

In this paper we do not attempt to improve the models of the upper chromosphere and transition region beyond the Fontenla et al. (1999) models, but we use the temperature versus height from them and only modify the photospheric layers. In subsequent papers of this series we will update the chromosphere and transition region parts of all the models using recent ultraviolet (UV) and extreme ultraviolet (EUV) observations and molecular lines. For now the layers above the photosphere should be considered only schematic, and consequently we do not include them in the tables in Appendix A.

We integrate the computed visible and IR spectra to obtain the total radiation flux from each model and assess the effects of the magnetic features on the solar flux in various wavelength bands. These results and the existing chromospheric models indicate interesting trends in the effects of magnetic fields on the solar irradiance and nonradiative heating.

## 2. INTERPRETATION

The density stratification used in our models results from an equation that has a similar form as the hydrostatic equilibrium equation but with added terms to account for large-scale motions, turbulent motions, and Lorentz forces similar to the terms shown in FAL02, equation (37) (which coincides with FAL93 eq. [1] for our current static models). Through the “turbulent pressure velocity” parameter,  $V_{\text{tp}}$ , we adjust the density stratification within certain bounds in order to account for processes not known in detail (see § 5.1). In our quiet-Sun models we assume for simplicity that the turbulent pressure velocity has the same value as the microturbulent line-broadening velocity,  $V_{\text{tb}}$ . Of course this is not necessarily true. In our active region models we do not use the same values for  $V_{\text{tp}}$  and  $V_{\text{tb}}$ , and we obtain the values of  $V_{\text{tp}}$  from other assumptions indicated in § 5.1. Our simplifying assumptions just reflect the difficulty obtaining diagnostics for the gas pressure scale height from existing observational data. Eclipse observations provide some data that are consistent with our quiet-Sun models, but there are hardly sufficient data, especially for active regions.

However, one can choose to interpret our one-dimensional models without regard to heights and instead only consider the relationship between gas pressure and temperature. The advantage of this scale is that it only involves local parameters of the gas that are not affected by  $V_{\text{tp}}$ , which is necessary to relate the gas pressure and density with height relative to an arbitrary zero. The disadvantage of a gas pressure scale is that it is possible that the same pressure may occur at two different heights of a one-dimensional atmosphere when velocities and Lorentz forces are present, but this is unlikely in the photosphere and chromosphere. Another alternative is the mass column density, but this is not a local property of the gas and it is related to the gas pressure through the pseudohydrostatic equilibrium equation, which involves  $V_{\text{tp}}$ .

It is known from the observations that the conditions in all layers of the solar atmosphere vary somewhat on timescales of several minutes. For instance, the well-known  $p$ -mode oscillations affect the photosphere and low chromosphere and produce an average profile of the weak absorption lines with a characteristic curved bisector. Detailed observations of low and mid-chromospheric lines (e.g., Balmer lines and Ca II K<sub>2</sub> and K<sub>3</sub>) also show changing profiles (e.g., Kneer & von Uexküll 1986; von Uexküll & Kneer 1995) and are related to the 3 minute chromospheric oscillations. The Ultraviolet Spectrometer and Polarimeter (UVSP) data for the Mg II  $h$  and  $k$  lines (with a

<sup>4</sup> See also <http://www.hao.ucar.edu/Public/research/fco.html>.

3 arcsec<sup>2</sup> pixel size) that form at the top of the chromosphere display about 10% asymmetric variations in the peaks with the 3 minute period (as found by one of us, J. M. F., in a 1989 unpublished study). Also, the UVSP Ly $\alpha$  data show more complicated but similarly small variations and some additional features due to transient cool material in the low corona (see Fontenla et al. 1988). The Solar Ultraviolet Measurements of Emitted Radiation (SUMER) data for upper chromospheric and transition region lines show motions at these frequencies and with amplitudes near the sound speed (Wikstøl et al. 2000). Sometimes very small areas experience sudden large brightening (microflares, e.g., Aschwanden et al. 2000) that is often attributed to sudden magnetic energy release (e.g., Falconer et al. 2000).

Our models do not reflect these variations but instead correspond to a “radiation average” of the less dynamic regions of each type. The parameters in our models are expected to differ somewhat from a strict Eulerian time average of varying physical parameters. These differences are small when the fluctuations are small, as in the photosphere, but can be very significant in the chromosphere. Thus, it is not meaningful to compare averaged temperature values at a given height from a time-dependent simulation to our model temperatures at that same height. Instead, the emergent radiation from a time-dependent simulation should be quantitatively compared with both high-resolution data and with medium-resolution observations such as those our models reproduce.

Our models are indeed not of instantaneous or average physical parameters but only of radiation-effective ones. The validation of our models rests on the comparisons with observations of the emergent radiation at the proper temporal and spatial resolution and can be considered a compendium of a large variety of observations, all at a certain resolution. Of course, the ultimate goal of atmospheric models is to obtain a complete and consistent physical description of all solar phenomena, in full agreement with all observations. Such a goal is not yet achieved, but our present models should be considered as a step in that direction.

More complete theoretical models will have to explain more details than are explained by the models we present here, such as the time-dependent and three-dimensional fine structure displayed by high-resolution images, as well as include full understanding of the physics behind chromospheric heating. Carlsson & Stein (1997) proposed that the passage of shocks with Mach numbers substantially larger than unity can produce a temporary several-fold temperature increase to account for the chromospheric emissions in nonmagnetic regions. At this point, it seems that this picture of chromospheric heating cannot explain the persistence of the quiet-Sun upper chromospheric emission lines observed at high temporal and spatial resolution (see Judge et al. 1997; Kalkofen 2001). Also, it is well known that there is a close relationship between enhanced chromospheric heating and magnetic fields (e.g., in the quiet network and active regions) and a less dynamic character in magnetic regions (e.g., Wikstøl et al. 2000), neither of which has yet been physically explained (but mechanisms have been proposed, e.g., by Fontenla [2005]).

### 3. SOLAR FEATURES AND MODELS

For the purpose of producing models of the main solar features observed on the disk we use a single model for each feature category. However, it should be kept in mind that a category represents a range of intensities in continua and lines and not a single value and that in the observations there may not be a sharp transition between these categories. By looking at an image one can always identify the features, but the pixels at the boundaries

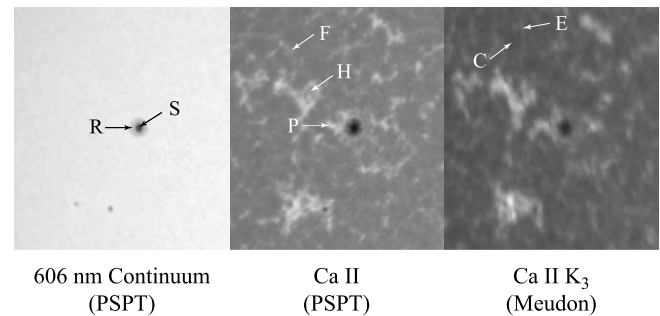


FIG. 1.—Images covering quiet-Sun network, active network, and active region features in the PSPT red and Ca II K broad bands, and in Ca II K<sub>3</sub> (data from the Meudon Observatory in 2005). The field of view is  $\sim 120'' \times 120''$ . While the PSPT images are simultaneous, the Meudon image was taken about 10 hr earlier.

display a gradual transition and there are also variations within each feature. Figure 1 shows typical images of quiet and active regions at about  $2''$ – $3''$  resolution and illustrates the chromospheric network structure and active region features we model. We show in this figure red-band and relatively broadband Ca II K images from the PSPT and a Ca II K<sub>3</sub> narrowband image from the Meudon Observatory.<sup>5</sup> From the two Ca II K images it is clear that the narrowband images display the network pattern with more contrast but in a more diffuse way than the broadband images. This is because the network lanes result from magnetic heating in mid- and high chromospheric layers that are better displayed in narrowband images, but narrowband images also show lower intensity emissions that occur in chromospheric and higher layers and even absorptions due to prominence material. We indicate in these figures the well-known categories of features we model and the arbitrary letters we assign to the models.

At the resolution of a few arcseconds that corresponds to these images, the quiet-Sun chromosphere observed in Ca II K images consists of a network structure of “network cells” surrounded by brighter areas known as “network lanes.” In continuum and white-light images (e.g., the PSPT red-band data) the active region areas may display very clearly defined sunspot umbrae, penumbrae, and faculae. Plage areas appear in both Ca II K images. We note that there is an overlap in some active region features because these definitions originate in observations of intensity levels at different wavelengths. In § 5 we clarify the definitions we used for defining separate models for each of the mentioned active region features.

### 4. QUIET-SUN FEATURES AND MODELS

Our quiet-Sun categories partially follow the VAL81 scheme. In that work the continuous distribution of intensities measured by *Skylab* in EUV lines and continuum was “discretized” by a set of models labeled A through F representing various bins in histograms of line intensities. However, for the purposes of our paper we do not find it necessary, or even convenient, to use so many categories. We use three categories that are known to be associated with certain characteristics of the magnetic field. These categories are labeled for historical reasons as C, E, and F, because they roughly correspond to those in VAL81. Our categories are described as follows:

C.—An area with the same intensity as the median in a histogram of a Ca II K image of a quiet area of the Sun. We find that

<sup>5</sup> See <http://bass2000.obspm.fr/home.php>.

the median is very close to the peak of the distribution but is statistically more stable. These intensities correspond to most of the central area of supergranular cells that are usually known as “quiet-Sun cell interior.”

E.—A bright area separating supergranulation (or network) cells, often called “network lane.” We describe this category as “quiet-Sun network.”

F.—Certain network lane areas that are much brighter than the average. We describe this category as “active network.”

Categories C and E are clearly not related to solar activity, but there are many studies that show correlation between brightness and magnetic fields in the quiet-Sun network. Small magnetic field elements are observed in the quiet Sun, and they usually display larger fluxes and mixing of polarities (or strong polarity gradients) at the network lanes. It is not clear whether category F contains a solar activity cycle component because these active network elements display magnetic element fluxes larger than the average network lanes. Also, sometimes it is possible to track them as the by-product of decay and fragmentation of active regions, as we observe in movies from PSPT Ca II K images taken over several consecutive days. Thus, it is not easy to establish if such bright network elements can exist independently of the solar activity cycle or only as a result of this cycle.

The network lanes are not clearly observed in the PSPT red continuum and are produced in chromospheric layers. Here we only study in detail the photospheres of the models, but because there are issues with the previously published E and F models we still retain these models here.

#### 4.1. Quiet-Sun Models

These models are based on the Fontenla et al. (1999) set of models, but we now modify the photospheres of models E and F to account for the absence of brightening in the quiet-Sun network lanes as observed in the PSPT red-band images. (This band contains continuum around 6060 Å with a few weak photospheric lines.) We found that the previous models E and F display significant unobserved contrast with respect to model C even at disk center ( $C_{\text{model}} > 0$ ). Thus, we revised the photospheric temperatures of these models to remain identical to those of model C up to slightly higher altitudes than before. The basic parameters for model C are unchanged from Fontenla et al. (1999), but we have introduced changes here in the elemental abundances that affect the electron densities because of the contributions of low first ionization potential (FIP) elements to the electron density.

The elemental abundances used in all our photospheric calculations are assumed to be height independent and are listed in Table 1. The photospheric layers of the models are not very sensitive to elemental abundances of high-FIP elements but are significantly affected by the changes to the low-FIP elements.

The abundances in Table 1 include reduced values for C, N, and O relative to those used by Fontenla et al. (1999) and also changes in low-FIP elements. Calculations of the semiforbidden C I line at 5381.833 Å vacuum wavelength, with  $gf = 0.02421$  according to the National Institute of Standards and Technology (NIST), shows good agreement with the Kitt Peak observations (Wallace et al. 1998). Therefore, the reduced C abundance is in agreement with our present models. Determination of the O abundance from OH weak lines, using other models, by Melendez (2004) yields a value compatible with the one we use. Also, our calculations of the O I resonance lines at 1027.4 and 1028.5 Å, formed in the chromosphere, are in better agreement with SUMER observations (Curd et al. 2001) when the reduced

TABLE 1  
ELEMENTAL ABUNDANCES IN THE MODELS

Element	Atomic Number	$\log(n_{\text{elem}}/n_{\text{H}})$	References
He.....	2	−1.00	
Li.....	3	−10.95	4
Be.....	4	−10.62	4
B.....	5	−9.30	1
C.....	6	−3.61	2
N.....	7	−4.22	4
O.....	8	−3.34	3
F.....	9	−7.44	1
Ne.....	10	−4.16	4
Na.....	11	−5.83	4
Mg.....	12	−4.47	4
Al.....	13	−5.63	4
Si.....	14	−4.49	4
P.....	15	−6.64	4
S.....	16	−5.16	4
Cl.....	17	−6.50	1
Ar.....	18	−5.82	4
K.....	19	−6.92	4
Ca.....	20	−5.69	4
Sc.....	21	−8.95	4
Ti.....	22	−7.10	4
V.....	23	−8.00	1
Cr.....	24	−6.36	4
Mn.....	25	−6.61	1
Fe.....	26	−4.55	4
Co.....	27	−7.08	1
Ni.....	28	−5.77	4
Cu.....	29	−7.79	1
Zn.....	30	−7.40	1

REFERENCES.—(1) Grevesse & Sauval 2000; (2) Allende Prieto et al. 2002; (3) Asplund et al. 2004b; (4) Asplund et al. 2004a.

abundance is used. When we examine the very weak photospheric O I lines near 6158.5 Å we find that a high O abundance would not be consistent with the Kitt Peak observations. Even the low value we use yields lines that are stronger than those observed.

The low abundances of C, N, and O have important effects on the molecular lines that are strong above the photosphere and in sunspots. For instance, these low abundances reduce the strength of the CN violet band with a head at 3883 Å unless the temperature minimum is lower than that shown in the present paper and given by Fontenla et al. (1999), as well as in FAL90, FAL91, FAL93, and FAL02. Weaker CN absorption is incompatible with the Kitt Peak observations (Wallace et al. 1998) and with an unpublished study of observations by one of us (J. M. F.). The low O and C abundances pose even bigger problems for CO lines with the temperature minimum shown in this paper. A lower temperature minimum was proposed by Ayres & Rabin (1996) based on CO observations. However, the quiet-Sun photospheric models are not substantially affected by the assumed C, N, and O abundances because they are determined by the visible and IR continuum spectra, which are practically unaffected by these abundances. Only photoionization edges from relatively high energy excited levels of these atoms affect these continua slightly. Thus, calculations of spectral lines from these elements using the present models are useful diagnostics of these abundances and will be used in conjunction with future observations.

Models C, E, and F are listed in Appendix A and include the temperatures and densities as functions of gas pressure. Heights are also listed for reference, but the height scale for one model can be arbitrarily offset from that of another model. The heights

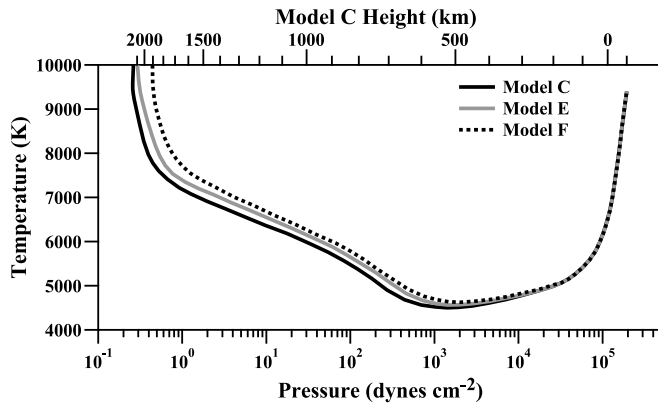


FIG. 2.—Temperature as a function of gas pressure for models C (quiet-Sun cell center), E (quiet-Sun network), and F (active network).

in the tables are measured from the height at which  $\tau_{5000} = 1$  because this has been common practice. However, we note that the zero height in each model is not geometrically constrained, and the height offset between the different models is unknown in our one-dimensional modeling.

In Figure 2 we plot the temperature as function of the gas pressure for the three models. The temperature increase with respect to model C starts at gas pressures of about  $10^4$  dyne  $\text{cm}^{-2}$  in model F and a bit higher in model E. For reference we also show for model C the arbitrary height scale in which the continuum optical depth at  $5000 \text{ \AA}$  is unity at the height zero. This arbitrary zero height occurs at gas pressure of  $\sim 1.16 \times 10^5$  dyne  $\text{cm}^{-2}$  for this model.

#### 4.2. CLV of Quiet-Sun Features

Figure 3 shows the CLV computed from model C in continuum windows at  $6060.5$  and  $15500.5 \text{ \AA}$  ( $0.2 \text{ \AA}$  bandwidth). The shorter of these wavelengths is representative of the red band observed with the PSPT. The intensities are computed at values of  $\mu = \cos \theta$  in decrements of  $0.1$  from  $1.0$ . The observed PSPT values are shown for the same  $\mu$  values interpolated (and extrapolated for the case of  $\mu = 1.0$ ) from the median intensity value for various intervals of  $\mu$ , namely, a circle  $\mu > 0.95$  and a set of annuli at intervals  $0.1$  centered at values of  $\mu$  of  $0.9, 0.8$ , etc. The median intensity value in each annulus is assigned to the  $\mu$  that corresponds to the annulus center of gravity, which is slightly shifted from the center of the  $\mu$  interval as described in Fontenla et al. (1999) (also see Appendix B). Also, the figure shows the CLV values from Pierce & Slaughter (1977) and Pierce et al. (1977) at nearby wavelengths of  $6000$  and  $15000 \text{ \AA}$ . As this figure shows, the model calculations in the red reproduce the observations within a few percent, and thus the temperature gradient at the photospheric layers responsible for the radiation at this wavelength is well represented by model C. At very small  $\mu$  ( $0.1$  and smaller), problems may arise because of observational limitations and also because the plane-parallel approach used in our emergent radiation calculations breaks down due to curvature effects. Again there is good agreement between the computed and observed CLV in the IR, within a few percent, but there is a slightly higher than observed computed value from model C near  $\mu = 0.4$ . We note that, according to the calculations, at around  $\mu = 0.4$  the IR continuum formation region overlaps with that of the red continuum at around  $\mu = 1.0$ , and thus a model change would affect the agreement with the observations in the red. Thus, the small disagreement is probably due to inaccuracy in the IR opacity (e.g., unaccounted departure from LTE in  $\text{H}_2^+$ ) or

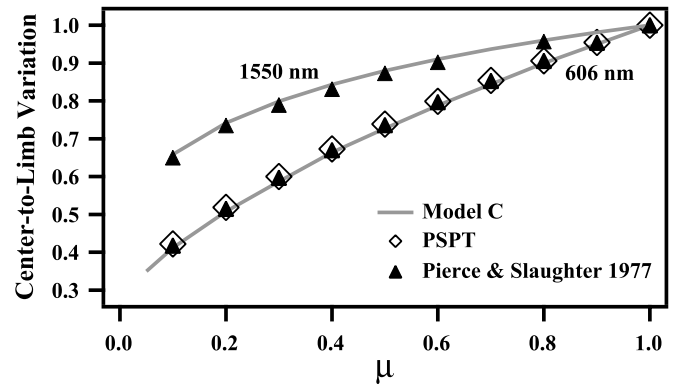


FIG. 3.—CLV computed from model C and observed by PSPT and by Pierce & Slaughter (1977) in the visible and by Pierce et al. (1977) in the IR.

to a somewhat different bandpass between the calculations and observations.

For models E and F the computed intensity contrasts between the quiet-Sun network models in the PSPT red band at most disk positions are below but very close to zero ( $-1\% < C_{\text{model}} < 0\%$ ). Observation of such small contrast is difficult, and we cannot rule out the need for tiny photospheric temperature or density variations that can change this contrast in the computations. These computed contrasts are not due to the photospheric layers, because for gas pressures greater than  $3 \times 10^4$  dyne  $\text{cm}^{-2}$ , we assume identical physical parameters for all quiet-Sun models. Instead, they are due to the differences at small optical depths in the layers above the photosphere.

#### 4.3. The Quiet-Sun Irradiance Spectrum

An important test of the combined quiet-Sun models is their ability to fit the observed solar irradiance spectrum. For this comparison we use only model C, because models C, E, and F have negligible differences in emitted radiation, and PSPT image analysis shows that more than 70% of the solar disk corresponds to model C. Since we have verified that the CLV computed from model C agrees with the observations, comparing the computed and observed irradiance amounts to testing the absolute values of the model temperature. Here we use the full solar irradiance spectrum from  $0.3$  to  $2.4 \mu\text{m}$  (included in the range of Thuillier et al. [2003] observations) with all lines computed using the approximate non-LTE (NLTE) procedure described in Fontenla et al. (1999) but now using the NIST atomic data,<sup>6</sup> molecular lines from Gray & Corbally (1994)<sup>7</sup> and HITRAN,<sup>8</sup> and improved values for continuum opacity edges arising from the most abundant elements. Our calculations use photoionizations not only from the ground level but also from excited levels. Also, we use photodissociation molecular opacities by OH, CH from Kurucz et al. (1987), and MgH from Weck et al. (2003).

At wavelengths outside of the visible and IR spectrum, and in the deep lines, the network contrast becomes significant because the emitted radiation forms in chromospheric layers. Thus, the irradiance spectrum computed from model C would be just a lower bound on the quiet-Sun irradiance spectrum, and it would be necessary to add the network component for computing the quiet-Sun irradiance spectrum accurately. Furthermore, solar irradiance observations at UV and at millimeter and longer wavelengths are very strongly affected by solar activity, and they

<sup>6</sup> See <http://physics.nist.gov/PhysRefData/ASD/index.html>.

<sup>7</sup> See <http://www.phys.appstate.edu/spectrum/spectrum.html>.

<sup>8</sup> See <http://cfa-www.harvard.edu/HITRAN/>.

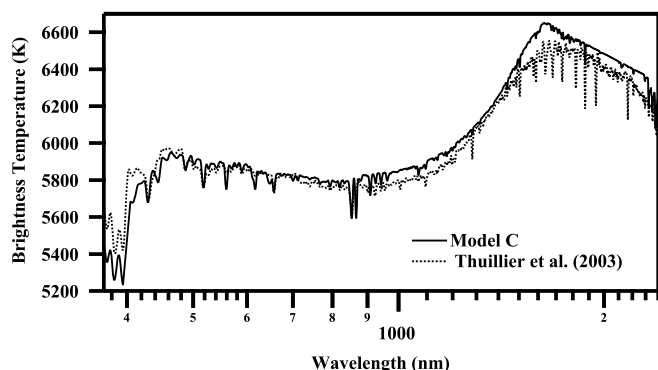


FIG. 4.—Computed 1 AU average disk brightness temperature, with resolution degraded to 5 nm, from model C and the composite observations by Thuillier et al. (2003).

are not directly comparable to the quiet-Sun models but require consideration of active Sun components. Since in this paper we are only concerned with the visible and IR, comparison of the computed model C irradiance at 1 AU with the absolute irradiance measurements described by Thuillier et al. (2003) is justified.

Our calculation resolves in full detail each of the lines we included (about 50,000 atomic lines and several hundred thousand molecular lines throughout the entire spectrum), but some observed minor lines are missing in our data because their atomic parameters are not found in the sources we used. In Figure 4 we show the computed and observed (Thuillier et al. 2003) irradiance spectra at 1 AU expressed in brightness temperature units (as described by Fontenla et al. [1999]). Both the computed and the observed spectra were convolved with a 10 nm half-width  $\cos^2(x)$  function truncated at the first zero. The instrument set that produced these observations was absolutely calibrated both in wavelength, by using reference lamps, and power, using a blackbody cavity at the Heidelberg Observatory (Mandel et al. 1998). The observations we use here were obtained on 1994 November, nearly at solar minimum, and have an estimated error of 3% in the measured irradiance. A comparison between these observations and earlier data from Neckel & Labs (1994) is shown by Thuillier et al. (2003). Also, the IR data at wavelengths longer than 1000 nm were subject to a smoothing procedure.

Figure 4 shows that the current computations yield a higher than observed continuum at long wavelengths and a lower one than observed at short wavelengths, below about 490 nm. The slight differences in the overall levels are produced by relatively small but noticeable photoionization edges in our calculations that may be based on incorrect atomic data. In particular, photoionization from many excited states of several elements (e.g., Si and Mg) are sometimes merged together in our calculations, although they have somewhat different wavelengths. Also, the smaller computed irradiance value compared with that observed around 400 nm results from the large value of the CH and OH opacities that we include, but if they are ignored, then the computed irradiance would be larger than the observed; apparently these opacities are important, but their current values are not compatible with the observations and their determination should be revised.

In Figure 5 we show two small wavelength intervals at 0.5 nm resolution to illustrate the agreement in detail, but we note that there is not a perfect match between the smoothing function we use and the instrument profile corresponding to the observations, which is variable and not well known at all wavelengths. This

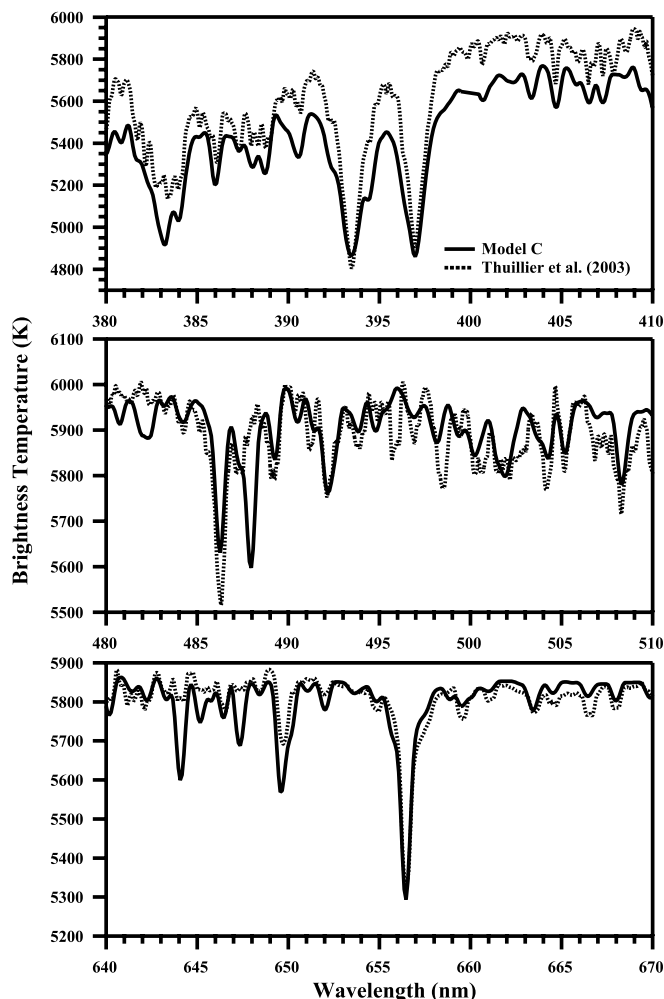


FIG. 5.—Clusters of lines from model C at 0.5 nm resolution and the composite observations by Thuillier et al. (2003).

figure shows that most of the computed spectral features in the solar irradiance at 0.5 nm resolution match those observed reasonably well, but there are some differences.

The comparisons in Figures 4 and 5 illustrate that the agreement between the computed and observed spectra for wavelengths longer than 430 nm is within the range defined by the probable error of the observations and abundances, and the uncertainty in the atomic data we used. However, there are systematic trends in that the computed irradiance is low between 336 and 490 nm and high between 293 and 325 nm and between 490 and 1300 nm. The method and atomic data we use for the full spectrum synthesis at this point are not accurate at short wavelengths where NLTE effects are most important. This is because the approximate NLTE method used for this synthesis (Fontenla et al. 1999) is not accurate enough at these wavelengths. While not included here, we currently perform more accurate computations for small wavelength intervals using complete full NLTE with partial frequency redistribution calculations (e.g., Ca II, Mg II, He, and H lines and continua). These computations, however, are not important for the photosphere.

We have also compared our computed full-resolution spectra for disk center with the Kitt Peak data by Wallace et al. (1998). We find general agreement in many photospheric lines and disagreements in the depths of strong lines that are most likely due to the approximate NLTE method we used for the full-spectrum

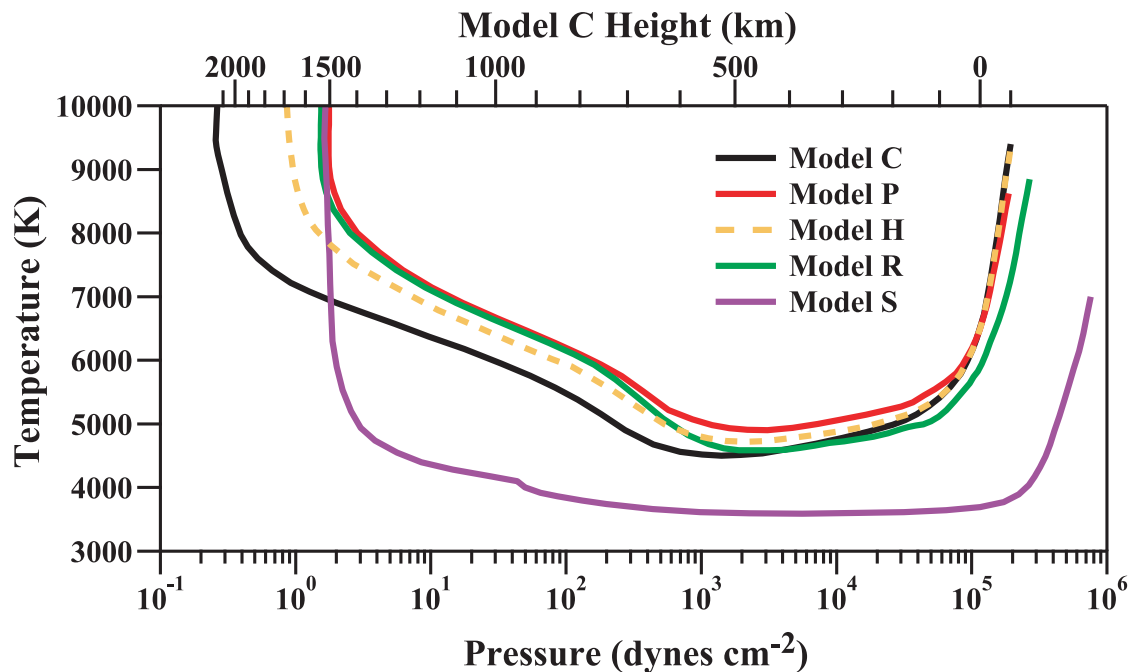


FIG. 6.—Temperature as a function of gas pressure for the active Sun models R (penumbrae), S (umbrae), P (faculae), and H (plage), compared to Model C.

calculation and/or needed improvements in the chromospheric layers of the models C, E, and F. Also, we find that a number of weak lines from heavy elements are not present in our calculations. Many of these missing lines are present in our database but do not have identified lower and upper levels and thus are not computed. Also, changes in the low chromosphere of our current models C, E, and F are needed to better account for the visible and IR molecular spectra of CN, CH, and CO if the abundances we used are correct.

Study of the discrepancies is ongoing, and we will improve our photoionization cross section values using the most recent data from Topbase (e.g., Cowley & Bautista 2003).<sup>9</sup> Also, future computations will include full NLTE effects in all relevant species. We expect that the new computation will explain the still unmatched edge around 325.5 nm and discrepancies between our computations and the observations in the range between 208.6 and 325.5 nm and will improve the overall agreement throughout the violet and UV spectrum. This portion of the solar spectrum is extremely complicated because of the merging of the very dense and deep absorption lines and the many photoionization continuum edges that are all far from LTE. After these improvements and the analysis of the low-FIP elemental abundances, we will reevaluate the need to introduce changes to the quiet-Sun models.

## 5. ACTIVE SUN FEATURES AND MODELS

Early models for active region features were developed by several authors, e.g., penumbrae by Kjeldseth-Moe & Maltby (1969), umbrae by Maltby et al. (1986), and faculae by Chapman (1977) and Walton (1987). Chromospheric models of plage were obtained by Lemaire et al. (1981) from *Orbiting Solar Observatory* 8 data. Also, recently high-resolution data have been used in studies of the fine structure in active region features, e.g., Malherbe et al. (2004).

We do not attempt to refer to all the research on these topics but point out that some faculae models have been proposed that resort to complex geometric effects due to subresolution fine

structure to account for the CLV in faculae, e.g., “hot wall” models of “flux tubes” by Spruit (1976). Recent high-resolution observations cast doubt on the existence of such “flux tubes”; e.g., Berger et al. (2004) write, “The main result of this study is that with  $\sim 100$  km resolution the majority of small-scale solar magnetic structure in this dataset is not resolved into discrete flux tubes.” Current simulations of magneto-convection, e.g., Keller et al. (2004), are promising, but they have yet to be improved by considering more realistic overall active region magnetic topology, exploring various boundary conditions, understanding quantitatively how the radiative energy flux is accounted for, and making quantitative comparisons with observations at all wavelengths. Keller et al. (2004) note, “Despite the excellent qualitative agreement between simulations and observations, there remain quantitative disagreements. . .” Also, these models have not yet been shown to quantitatively account for all the moderate-resolution observations that our models discuss, and we consider a discussion of such models beyond the scope of this paper.

In our previous work, Fontenla et al. (1999), we discussed three components of solar activity, namely, “average plage,” “bright plage,” and “sunspot umbra.” However, our more recent work on modeling the observed solar irradiance variations (e.g., Fontenla et al. 2004) showed that penumbrae areas are very important for this modeling, at least in solar cycle 23. Consequently, in this paper we add a new model for sunspot penumbra, and the set of solar activity features for which we construct radiation-effective one-dimensional model atmospheres is as follows:

- R.—Sunspot penumbra,
- S.—Sunspot umbra,
- P.—Faculae,
- H.—Plage.

Figure 6 shows the temperature as a function of gas pressure for these four models together with model C shown for reference. The photospheric part of these models is listed in Tables 6–9; we remind the reader that the height scale can be arbitrarily offset and that there is no correspondence between any particular heights in the different models.

<sup>9</sup> Also see <http://vizier.u-strasbg.fr/topbase/>.



### 5.1. Density Stratification

An important issue, especially with the active feature models, is how the magnetic field affects the density stratification. Detailed physical consideration of this issue is beyond the scope of the present paper and depends on the details of the MHD processes at work. As was mentioned before, in our previous work (see FAL02, eq. [37]), we used a scheme by which we compute the scale height of the material including the turbulent pressure velocity,  $V_{\text{tp}}$ . This parameter was introduced to describe the effects of turbulent motions on the stratification and has the form of a Bernoulli term (see FAL93). However, the same parameter can also be used to describe effects of the magnetic field, or more properly the Lorentz force, in the density stratification. In our plane-parallel case the stratification is given by the equation

$$\frac{d}{dz} \left( \frac{\rho V_{\text{tp}}^2}{2} + \rho U^2 + p_g \right) = -g\rho, \quad (1)$$

where  $p_g$  is the gas pressure,  $U$  is the mass velocity (we set this to zero in our current models), and  $V_{\text{tp}}$  is the turbulent pressure velocity. By defining the “effective” gas pressure,  $p_{\text{eff}}$ , and using the isothermal sound speed,  $V_{\text{si}} = (p_g/\rho)^{1/2}$ , where  $\rho$  is the mass density, this equation can be transformed to the following,

$$\frac{dp_{\text{eff}}}{dz} = -\frac{gp_{\text{eff}}}{(V_{\text{tp}}^2/2 + U^2 + V_{\text{si}}^2)}, \quad (2)$$

which has the simple solution

$$p_{\text{eff}} = p_{\text{eff}}(\xi_0) e^{-(\xi - \xi_0)}, \quad (3)$$

with

$$d\xi = \frac{gdz}{(V_{\text{tp}}^2/2 + U^2 + V_{\text{si}}^2)}. \quad (4)$$

The Lorentz force can also be expressed by the parameter  $V_{\text{tp}}$ , and in some cases this value can be comparable to the Alfvén velocity. For instance, if one assumes negligible magnetic tension and that the Lorentz force can be described by only the magnetic pressure, then the stratification equation is

$$\frac{d}{dz} \left( \frac{B^2}{4\pi} + p_g \right) = -g\rho \quad (5)$$

if we ignore other effects and the velocities. This equation can be expressed in the previous form by assuming

$$\frac{V_{\text{tp}}^2}{2} = \frac{B^2}{4\pi\rho} = V_A^2, \quad (6)$$

where  $V_A$  is the Alfvén velocity. However, we note that in general the magnetic tension must be included, and in many cases (in a potential field or in a so-called force-free field) the magnetic tension exactly balances the magnetic pressure term. The purpose of the example above is only to illustrate the similarity between the ad hoc turbulent pressure velocity and the Alfvén velocity in some cases.

In our previous papers, and here for the quiet-Sun models, the turbulent pressure velocity was set equal to the microturbulent velocity that broadens the line profiles. The microturbulent velocity is usually regarded as due to unresolved motions needed

to account for the increased line broadening over that expected from thermal atomic motions only and is especially important for heavy elements. For the active region models in this paper we have reduced the microturbulent line-broadening velocity to account for the observations of narrower spectral lines reported in the literature, but depending on the case and altitude, we increase the turbulent pressure velocity to account for the effects of the magnetic field on the density stratification. Thus, we choose a relatively high and decreasing turbulent pressure velocity for the stronger magnetic field regions in an attempt to describe an increased height scale due to the magnetic forces. However, this issue is very complicated, and a better treatment requires a consistent physical model of the MHD in active regions considering the momentum and energy balance. Such analysis must consider radiative energy transport in all layers, including the photosphere where radiative energy transport is essential and where the diffusion approximation does not apply for the radiative flux. Given the complicated nature of the problem, we adopt here ad hoc empirical values that are primarily chosen to match the observed intensities at many wavelengths and disk positions. Secondly, we assume an approximate horizontal gas pressure equilibrium between all models at a gas pressure of  $\sim 1.9 \times 10^5$  dyne  $\text{cm}^{-2}$ , which corresponds to the base of model C, and look for only small differences of the  $\tau_{5000} = 1$  height level, as suggested by the observations. The last of these criteria probably applies to faculae but is dubious in the penumbra models and not very significant for the umbra model. In this last model the  $1.9 \times 10^5$  dyne  $\text{cm}^{-2}$  gas pressure value occurs above the  $\tau_{5000} = 1$  level and where Lorentz forces are probably large (the plasma  $\beta$  is near unity). There are currently insufficient observational constraints on  $V_{\text{tp}}$  and thus much arbitrariness in our choice of values.

### 5.2. Sunspot Penumbra Model

Model R was built to represent an average penumbra at moderate resolution. High-resolution data are available at some wavelengths and show very interesting fine structure and flow patterns that are beyond our present effort to develop a medium-resolution radiation-effective model. We discuss here some peculiarities of the limb darkening as they seem to relate to the horizontal structure of the penumbra and the Evershed flows at a scale much larger than that of the fine details.

We base our penumbra model, R, on the data from del Toro Iniesta et al. (1994) and Kjeldseth-Moe & Maltby (1969). These were complemented with PSPT observations of the red continuum and Ca II K and with published data. We have also considered the model published by Ding & Fang (1989), but as noted by del Toro Iniesta et al. (1994), these models propose a very low photospheric temperature that is not consistent with the observations. At the red continuum (6060.5 Å) our model produces, at disk center, a contrast of  $-0.2$  with respect to model C that is consistent with published values and our PSPT observations.

We adjusted the temperatures in the deepest layers in our model to values somewhat lower than in the quiet Sun (and also lower than in faculae) at the same gas pressure in order to match the observed contrast with respect to the quiet Sun at IR wavelengths (contrast  $\sim -0.1$  at  $1.55 \mu\text{m}$ ). From the lower temperature, one expects the scale height in sunspot penumbrae to be lower than in the quiet Sun and even lower in umbrae. For the umbra, the well-known Wilson depression leads to a lower absolute height for the layer at  $\tau_{5000} = 1$ . However, it is very hard to determine differences in the absolute height from the observations alone, especially in the inhomogeneous (even at moderate resolution) penumbra. Also, the magnetic field is supposed to change strongly with height, and significant Lorentz forces are expected (e.g., see

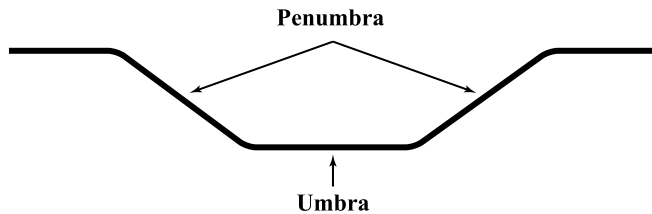


FIG. 7.—Geometric structure of penumbra.

Kjeldseth-Moe & Maltby 1974) in addition to the observed large-scale Evershed flows whose vertical variation is not well known.

We observed systematic variations of brightness in the penumbra in observations of penumbra in the PSPT red band. The observations correspond to large, approximately round and simple spots that display almost annular penumbra. Besides a gradual decrease in intensity from the outer to the inner penumbral edge, we observe that when the sunspots are not at disk center the part that is closer to disk center is systematically darker than the part that is farthest from disk center. We interpret this observation by a geometric effect in which in addition to vertical temperature stratification, there is also a horizontal variation. This variation is consistent with an isobaric surface having a wide “funnel” shape as shown in Figure 7. This funnel shape of the isobaric surface, in combination with a temperature decrease with decreasing gas pressure, would explain the observed effect. In the few cases we measured, the slope of the isobaric surface with respect to the horizontal is about 5% and is probably consistent with the Wilson depression of the corresponding umbrae, but more comprehensive statistical studies are necessary. This funnel shape is qualitatively consistent with the observations by Balthasar & Collados (2005) that used a very different analysis.

### 5.3. Sunspot Umbra Model

Model S is built to represent an average sunspot umbra at moderate resolution. High-resolution data show umbral dots and structure that are beyond our present effort to develop a radiation-effective model of medium scale. The question of differences between sunspots was addressed by Maltby et al. (1986), but we think it should be studied further by comprehensive statistical analysis of more solar cycles. Also, it is well known that even at a resolution of several arcseconds there are significant variations of intensity within the sunspot umbra, and these variations can be greater than 10%. Thus, we present here a model based on a “typical” umbra location and do not attempt a more comprehensive description of the variations.

Starting with the Fontenla et al. (1999) umbra model, we made significant changes, due to the changes in abundances, to obtain agreement with the observations of Maltby et al. (1986). Also, we improved the previous model by considering 15 levels of the H atom instead of the previous five levels, by modifying  $V_{\text{tp}}$  for expanding the density stratification that is affected by Lorentz forces, and by introducing some other variations in the temperature versus gas pressure function for reproducing the observed CLV of the contrast with respect to model C.

An important limitation in the observation of sunspots is that due to their large contrast with their surroundings, instrumental scattered light may decrease the measured value. Thus, we do not use PSPT data for estimating the contrast or constraining the CLV but rather refer to the data used by Maltby et al. (1986). The ratio of the intensity at disk center calculated for models S and C and averaged over a  $0.2 \text{ \AA}$  FWHM bandpass is 0.066 at  $6060.5 \text{ \AA}$  and 0.52 at  $15500.5 \text{ \AA}$ , which corresponds to the “mid”

case, M, in Maltby et al. (1986). However, a source of uncertainty is the unknown details of the bandpass used by the observations, since in sunspot spectra, there are molecular lines near these wavelengths that can introduce some dependence on the bandpass of the observed values.

Other modifications to the Fontenla et al. (1999) umbra model are the lower height of the transition region and much lower temperatures at chromospheric layers. These changes practically eliminate the chromosphere and are an early attempt to reproduce the single-peaked (i.e., lacking any central reversal) observed profiles of the lines of Ca II H and K (see Ding & Schleicher 1998), Mg II h and k (J. M. Fontenla 1992, unpublished; Morrill et al. 2001), and Ly $\alpha$  (see Fontenla et al. 1988). Our chromospheric umbra model will be addressed in more detail in later papers.

### 5.4. Faculae and Plage Models

Various authors use different, and sometimes unclear, definitions of faculae and plage. Historically, faculae were first discovered around sunspots in white-light images (Secchi 1865) that correspond mostly to visible continuum photospheric radiation, and plage were observed in filtergrams taken in H $\alpha$  and Ca II K (e.g., Ellison 1952; Dodson 1954, respectively), which are formed in chromospheric layers. Faculae are also bright in the Ca II line, and they can also be regarded as bright plage, which is the source of our notation of “bright plage” in Fontenla et al. (1999). However, from now on we define in our work “faculae” as the parts of active regions that are brighter than the quiet Sun at red continuum wavelengths at disk positions with  $\mu < 0.5$  and “plage” as those parts that are visible in chromospheric lines, e.g., in the K<sub>3</sub> and K<sub>2</sub> features of the Ca II line but are not visible in the red continuum.

Our models P and H, for faculae and plage, are modified versions of those by Fontenla et al. (1999) for “bright plage” and “average plage,” respectively. Model P in that paper and in FAL93 was based on the Lemaire et al. (1981) data and models.

We have modified our previous model P near the level of  $\tau_{6060.5} = 1$  to produce an almost zero contrast, with respect to model C, at disk center for this wavelength corresponding to the PSPT observations. In our current calculation the model P emergent intensity at  $6060.5 \text{ \AA}$  and  $\mu = 1$  is 0.3% higher than for model C, but a calculation with a slight difference in the opacity estimate can very well produce a small but different contrast, and even one having an opposite sign. Thus, the exact value is not significant below about 1%; therefore, our model P contrast at disk center is effectively zero.

Also, in the current paper we do not assume a fixed relationship between the turbulent pressure velocity and hydrogen density, as was used in Fontenla et al. (1999) and described in FAL91. In our current model the turbulent pressure velocity was decreased below and near the temperature minimum from its previous values to values close to those of model C, and as a result there is a slight reduction of the chromospheric H density and pressure. Other modifications were carried to produce the contrast with respect to model C that is observed in the PSPT red band and other data, as shown in § 5.4.

Our model H was revised in such a way that the contrast with respect to model C at  $6060.5 \text{ \AA}$  is practically zero at all disk positions. This was done for consistency with the PSPT red-band observations. At layers below that where  $\tau_{6060.5} = 1$  we adopted the same temperatures as in model C because published observations we reviewed (e.g., Sanchez Cuberes et al. 2002) suggest that only facular areas have a significantly different (lower) intensity at IR wavelengths. However, this issue remains to be studied with better statistics using simultaneous observations at multiple wavelengths.

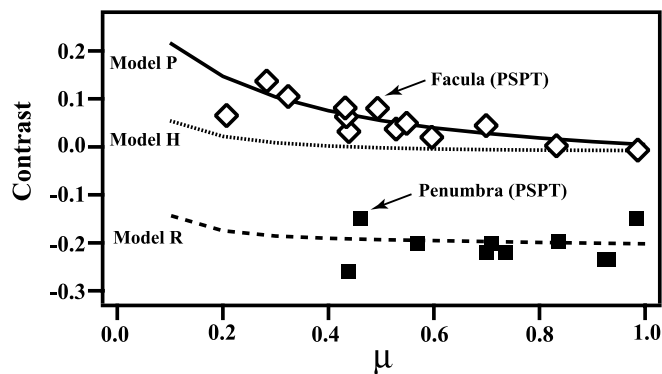


FIG. 8.—Computed and observed contrast of active feature models relative to the quiet Sun at the PSPT red band and its CLV.

### 5.5. Active Sun Features Contrast and CLV

The characterization of the contrast of active regions with respect to the quiet Sun at all disk positions is complicated by the lack of observations of the same active region at locations on the disk that cover the entire range of  $\mu$  from 1 to 0.2 (the smallest  $\mu$  at which we can neglect curvature effects). In addition, when a feature is tracked across the solar disk the intrinsic temporal evolution cannot be isolated from the CLV behavior. Because of all this, and practical limitations with the data, we only measure a number of cases from the available PSPT data.

Figure 8 shows the contrast with respect to model C as a function of  $\mu$  for the various solar activity features at a wavelength representative of the red band of the PSPT instrument. The PSPT observations of a few cases are also shown, but the intrinsic variations between these data can be very significant. The computed intensity ratio of the penumbra model R to model C is 0.8 with very little CLV, consistent with observations by the PSPT instrument. Smaller ratios of up to 0.7 have also been reported and are also consistent with values we find at some penumbral locations within the PSPT data. The value we used above corresponds to most of the observed central portions of the penumbra between the umbra and the areas surrounding the penumbra in the simple spots we studied.

The sunspot umbra computed contrast at 6060.5 Å is nearly constant, in agreement with Maltby et al. (1986). The contrasts of models P and H with respect to model C at this wavelength are practically zero at disk center but increase toward the limb, i.e., models P and H have a slower emergent intensity decrease than model C with decreasing  $\mu$ . Model P reaches a contrast of  $\sim 10\%$  at  $\mu = 0.3$  in agreement with the PSPT observations. A very small contrast, of a few percent with negative or positive sign, can be sometimes observed at disk center in PSPT data. This is explained by the sensitivity of the crossover between the temperatures versus gas pressure curves shown in Figure 6. A small change in any atmospheric parameter between different facular areas can produce small contrast variations at disk center.

Figure 9 shows the contrast and its CLV at an IR continuum wavelength of 15500.5 Å. At this wavelength, except at  $\mu < 0.4$ , model P has a negative contrast, as was shown by Fontenla et al. (2004) using the previous Fontenla et al. (1999) model. These previous results are affected by our current modifications to this model, but we still obtain a behavior in which model P relative to model C is dark at disk center and bright near the limb. The comparison with the observations by Sanchez Cuberes et al. (2002) shows that the present model is close to the observations (for  $g = 1.5$ , which corresponds to all facular areas; see their eq. [3] for the definition of  $g$ ) except very close to the limb for  $\mu < 0.2$

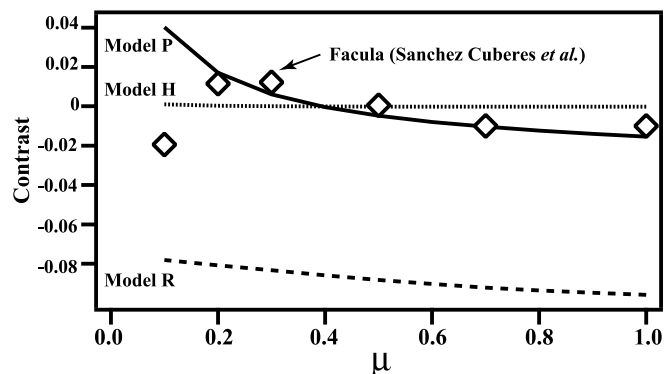


FIG. 9.—Computed contrasts of active feature models relative to the quiet Sun in the 1.55  $\mu\text{m}$  continuum and its CLV compared with the Sanchez Cuberes et al. (2002) faculae observations.

where the plane-parallel horizontally uniform model calculations would not be accurate. The current model crosses zero contrast at  $\mu = 0.4$ , which is somewhat closer to the limb than the observed crossing. According to our calculations the radiation at this wavelength and  $\mu$  value is produced practically at the same layer at which optical depth at 6060.5 Å is unity at  $\mu = 1$ . Consequently, a decrease in the temperature of this layer such that the IR data would be matched may result in a mismatch at the visible. Thus, it is likely that the small difference between our calculations and the IR observations reflects a small inaccuracy in the IR opacity near this layer (e.g., unaccounted departure from LTE in  $\text{H}_2^+$ ) and not a change in the photosphere temperature. For umbra, the ratio of model S to model C intensity at 15500.5 Å (not plotted) is  $\sim 0.52$  at disk center, decreases slightly toward the limb to 0.42 at  $\mu = 0.3$ , and is consistent with the observations by Maltby et al. (1986).

The current plage model yields practically zero contrast (unit intensity ratio) for model H with respect to C because of our assumption of identical temperature versus gas pressure in models H and C in the deep photosphere. Again, tiny contrasts of either sign may be produced by very small variations in the photospheric gas pressure, temperature, or opacity.

## 6. EMITTED FLUX

The comparison between active and quiet-Sun models shows that magnetic fields have two opposite effects on different parts of the solar atmosphere. This is shown by the crossings of the temperature versus gas pressure curves in Figure 6 where almost all active region models cross the model C curve. These crossings, discussed below, occur at very different gas pressures ranging from those typical of the quiet-Sun photosphere up to the mid-chromosphere (our present chromospheric models are only schematic). Thus, the effects of magnetic heating follow a progression in which magnetic heating becomes effective at decreasing pressures in active region models.

In sunspot umbrae the crossing occurs high in the atmosphere at low gas pressures, since the observations indicate that the temperature remains depressed up to pressures  $< 10 \text{ dyne cm}^{-2}$ , which correspond to the model C chromosphere. At transition region layers, as shown in FAL90, FAL91, FAL93, and FAL02, local heating is not needed to explain the observations, but the downward energy flux from the magnetically heated corona can produce similar EUV emissions to those in active regions. However, despite the large values of the magnetic field, little or no magnetic heating seems to occur at gas pressures between 10 and 1000  $\text{dyne cm}^{-2}$ , as is shown by the weakness of most

TABLE 2  
RADIATION FLUXES BETWEEN 400 AND 5000 nm

FEATURE	RADIATION FLUX (W m <sup>-2</sup> )				
	400–5000 nm	400–500 nm	500–600 nm	600–1000 nm	1000–5000 nm
C.....	5.974E+7	9.084E+6	8.900E+6	2.188E+7	1.988E+7
E.....	5.954E+7	9.039E+6	8.851E+6	2.178E+7	1.987E+7
F.....	5.963E+7	9.07E+6	8.867E+6	2.181E+7	1.988E+7
H.....	6.162E+7	1.009E+7	1.009E+7	2.188E+7	1.988E+7
P.....	6.176E+7	9.613E+6	9.265E+6	2.282E+7	2.007E+7
R.....	4.966E+7	3.213E+5	6.967E+6	1.839E+7	1.794E+7
S.....	1.243E+7	6.367E+6	5.89E+5	3.814E+6	7.704E+6

chromospheric emissions (e.g., the lines in the 1300–1400 Å spectral range shown by Curdt et al. [2001]), in addition to the lack of Ca II (e.g., Ding & Schleicher 1998), Mg II (J. M. Fontenla 1992, unpublished; Morrill et al. 2001; also see Fig. 7 in Lites & Skumanich 1982), and Ly $\alpha$  (e.g., Fontenla et al. 1988) central reversals. Over sunspots the temperature must rise very quickly from temperatures near 4000–5000 K directly to coronal values. Of course, at and below photospheric layers there appears to be a large suppression of energy flux from below.

In sunspot penumbrae the crossing occurs at gas pressure of several times  $10^3$  dyne cm<sup>-2</sup>, i.e., around the model C temperature minimum. Penumbrae have significantly bright chromospheres, as is shown by strong and centrally reversed Ca II, Mg II, and Ly $\alpha$  emission cores. Thus, despite the lower magnetic field compared with umbrae, magnetic heating occurs at higher pressures and consequently is more effective than in umbra. The inhibition of the energy flux from below is less severe, as shown by the much less depressed temperature than in umbrae at and below the photosphere.

In facular areas the crossing occurs at gas pressures near  $10^5$  dyne cm<sup>-2</sup>, which corresponds to the model C photosphere slightly above the  $\tau_{5000} = 1$  level. The trend continues; the magnetic field is smaller, but the magnetic heating is more effective than in the penumbrae. Here the energy flux at deep photospheric layers is even less depressed than in the penumbra.

In plage areas and in the network there is not a clear crossover, since there appears to be no significant energy flux inhibition in the deep photosphere. In these cases the magnetic heating becomes effective at low chromospheric layers and seems to increase with the magnetic field strength, as is suggested by reported correlations of Ca II K<sub>3</sub> line strength with magnetic flux (e.g., Schrijver et al. 1989).

In the photosphere one expects that the magnetic field in sunspot umbra, and to a lesser extent in penumbra and active regions, suppresses convective energy flow. This can explain the lower temperature at the base of the active region models. However, it is not clear whether this process is significant within photospheric layers because there the energy transport is supposed to be due to radiation.

It does not appear that, in general, the magnetic heating depends exclusively on the field strength or radial flux, because the opposite trend is found in umbrae, penumbrae, and faculae, as mentioned above. Instead the different dynamics and the inclination of the field vector with respect to the vertical are likely important factors. Observations of faculae and sunspots indicate that horizontal fields have much less effect than vertical fields on inhibiting mechanical energy flux from the deep layers and that this flux together with the local magnetic field seems essential

for magnetic heating of the chromosphere. A simpler relationship between the heating and the field strength may hold only when the magnetic field is weaker and does not seem to inhibit the heat flux in the deep photosphere.

Table 2 shows the total radiative energy flux for each of the models. These quantities show the effects of magnetic fields on the solar output at wavelength bands in the visible and IR and over the whole range. Using the relative areas inferred from PSPT images in Ca II K (0.706 for model C, 0.258 for model E, and 0.036 for model F), the total radiation flux for the quiet Sun in the band 400–2300 nm is  $5.732 \times 10^7$  W m<sup>-2</sup>. The inferred radiation flux at the Sun from the Thuillier et al. (2003) irradiance observations in a corresponding band is  $5.606 \times 10^7$  W m<sup>-2</sup>. Thus, our computed quiet-Sun flux is 2% above the measured value in this band and within the accuracy of the observations and our atomic data.

As Table 2 shows, the faculae model produces an increased emitted flux at most wavelengths, but the relative increase diminishes as the wavelength increases. This is consistent with the observations and is an indication of the magnetic heating occurring predominantly at low-pressure layers that have more influence on the lines than in the continuum. This is also consistent with the low contrast of faculae at IR wavelengths near 1600 nm (the minimum H<sup>-</sup> opacity) that show that deep photospheric layers are insensitive to magnetic heating.

In the band 400–5000 Å, which comprises most of the radiative energy flux, model P radiates an excess of about  $2.0 \times 10^6$  W m<sup>-2</sup> over model C (about 3% of the total radiative flux). Geometric effects such as “hot walls” can explain an angular, and sometimes a wavelength, redistribution of the radiation flux due to inhomogeneities at relatively small horizontal scales. However, by definition, radiative energy balance over larger features produces the same outward radiative energy flux at any solar radius and thus would require an increased radiative flux present at the top of the convective layers underneath faculae to explain the excess radiation in faculae and plage. Such an increased convective flux is contrary to the usual view in which the magnetic field reduces convective transport underneath active regions. Instead, dissipation of magnetic free energy is a possible source for compensating a somewhat reduced convective flux underneath and supplying energy for the increased emergent radiative flux.

## 7. DISCUSSION AND CONCLUSIONS

The models presented here provide reasonable but simplified explanations for a large number of medium-resolution solar observations. Thus, these models provide a way to estimate the physical parameters of the solar atmosphere in the quiet-Sun network and in active regions. However, the models are a discrete

representation of a wide range of characteristics, and each model represents (but is not identical to) a range of conditions in the Sun.

Our quiet-Sun models are validated through a number of observations. In particular, the comparison of the observed spectral irradiance (Thuillier et al. 2003) with that produced by the model provides an absolute scale. This comparison is presented here and shows that the combination of our quiet-Sun models reproduces the observed visible and IR spectral irradiance. The differences between the computed and observed irradiance brightness temperature are within a few percent, but in some line-dominated regions somewhat larger differences occur especially at short wavelengths. Some of these differences are due to unknown atomic parameters for certain lines, and other differences seem related to incorrect or missing photoionization atomic data.

The present photospheric models are very useful in obtaining estimates of the solar spectral and total irradiance and their variations. As shown in this paper, the entire visible and IR irradiance spectrum is well described by our models, at least in the range 0.4–3  $\mu\text{m}$ , except for some small details. These details range from differences in the continuum level to the cores of deep chromospheric lines. They are sometimes due to inadequacy of the current chromospheric layers and other times apparently due to lack of accurate atomic data, lack of full NLTE computations in all species, and issues with certain abundances. Comparison between the spectral irradiance variations observed by the Spectral Irradiance Monitor instrument (Harder et al. 2005) and the synthesis method (Fontenla et al. 1999) using the current models will be addressed in future papers.

We also show here that at least in the range we consider there are no significant “missing” opacities, in agreement with Kurucz (1992b), because most of the previously identified problems have been solved more recently by including the CH, OH, and MgH photodissociation continua from excited vibrational levels (as suggested by Tarafdar & Vardya [1972]), and by photoionization continua from low-lying excited levels of many elements. We now include the most important of these opacity sources but find that at around 400 nm they seem too high and produce an unobserved decreased irradiance. Also, we find significant problems with the opacity at a few seemingly well-defined edges at about 490 and 325.5 nm, at which we probably have inaccurate photoionization cross section values. We continue to improve the atomic data and, in particular, the photoionization continua using the more recent calculations from Topbase. These improvements in our calculations are not trivial because we need to consider each of these continua in great detail for each ion, level, and sublevel, considering accurate wavelengths. As the available atomic data used improve, we will perform minor adjustments in the models to improve the agreement with the observations.

The synthesis method described by Fontenla et al. (1999) presented a frame for the application of the models presented here to study the solar irradiance. In the computation of the complete solar spectrum shown here we use full NLTE computation only for hydrogen, and we carry out an approximate NLTE method, as is described in that paper for computing the whole spectrum. This approximation is reasonably accurate for visible and IR wavelengths, but certainly it is not good enough at short wavelengths. We are currently working on eliminating the use of the approximate NLTE for the spectral synthesis and instead carrying out full NLTE computations for all elements. This will improve our synthesis at short wavelengths and also permit us to compute the UV solar spectrum in full detail.

Also, our models provide a way to quantitatively estimate the effect of the various levels of magnetic activity observed on the

solar disk on the radiative losses. The differences between the models indicate a progression in the gas pressure at which magnetic heating starts being significant. In sunspot umbrae this heating deposits only a small amount of energy at the low-temperature chromospheric layers. In the penumbra, the heating affects higher pressure layers at values around those of the quiet-Sun temperature minimum and produces a chromosphere with line emissions similar to those of the active regions. In the active regions surrounding sunspots, the magnetic heating occurs much earlier and at very high pressures typical of the photosphere. Thus, magnetic heating is more effective in active regions than in umbrae despite the lower magnetic field magnitude.

The inhibition of energy flux shown by the decreased deep photospheric temperatures relative to the quiet Sun appears related to the reduced magnetic heating with increasing field magnitude in many active region features. This suggests that the upward energy flux plays an important role in the magnetic heating. The sequences shown by the observations and reflected in our models are not consistent with a direct relationship between magnetic field strength and magnetic heating. Also, there is a clear ambivalence in the effects of the magnetic field in that it favors an increased temperature in some layers and a decreased temperature in others.

We think that the reason for the different characteristics of the magnetic heating in umbra, penumbra, faculae, and plage is the different magnetic field geometry in them and not just the field strength. Mostly horizontal fields are present in heated layers, while mostly vertical fields are present in cool regions. Thus, a magnetic heating mechanism needs to consider the field geometry and explain the characteristics and trends we describe in this paper.

Magnetic heating mechanisms should enable quantitative validation by expressing the heating as a function of the relevant physical parameters. When such a specification is available we should be able to compute models in which the temperature structure is derived instead of the present set in which the temperature structure is arbitrarily chosen to fit the observations.

We caution readers not to use partial specifications of our models, e.g., just the heights and temperatures, in other codes for computing the emitted spectra. Our model listings include the turbulent pressure velocity and the electron, proton, and H atom densities. We have included in this paper the elemental abundances we used. All these values should be used consistently to apply our models. Use of other abundances or densities derived from different approximations changes the models.

Penza et al. (2004) used values from Fontenla et al. (1999), together with the program by Gray and Corbally (1994), for computing the emitted intensity. They found that their emitted intensity computations yielded a negative contrast of model P with respect to model C at 6060–6070 Å wavelengths. This contradicts our calculations using the complete models that show a positive contrast of these models at those same visible wavelengths at disk center and increasing at other positions. The reason for the discrepancy is most likely that the code they used does not take into account all our densities but computed them in LTE with elemental abundances that slightly differ from ours. Small differences in the densities, and especially in the electron density, would produce differences from our  $\text{H}^-$  and other species opacities and thereby from our emergent intensities. These differences are likely to be of only a few percent and should not be considered significant but can lead to conflicting results when small differences are examined, as those we mentioned above. The use of our complete models, including densities, improves the agreement between different calculations, although minor differences can still occur due to

different atomic data, interpolation procedures for tabulations, or other approximations.

Our model tabulations include the NLTE departure coefficients for  $H^-$  when different from unity (in model S), as well as the  $H$  ionization computed in NLTE. Near the photosphere the departures from LTE are small, but the contributions of the NLTE upper photospheric and lower chromospheric layers to the integrals that determine the optical depth and the emitted intensity can have minor effects on the emitted intensity. Our computations are based on two codes, namely, the Solar Radiation Physical Modeling (SRPM) code developed in C++ by Fontenla et al. (1999) and the PANDORA code developed in FORTRAN by Avrett & Loeser (2003). In addition to using different languages, these codes use different approximations for the NLTE, emergent intensity, and radiative loss calculations. However, we routinely compare results from both codes and only find minor differences that are fully explained by the different approximations. In particular, PANDORA uses opacity sampling based on line data from Kurucz (1992a)<sup>10</sup>

<sup>10</sup> See <http://kurucz.harvard.edu>.

to account for the many photospheric lines, while SRPM computes the lines given by NIST in detail using the approximate NLTE method discussed by Fontenla et al. (1999). These different approximations turn out to be somewhat significant for evaluating the radiative flux and radiative losses. We believe that the sampled opacities are less accurate for this purpose, and therefore, we have used SRPM for the calculations of these quantities. Also, the detailed wavelength dependence of the SRPM opacities permits us to compute and compare with observed high-resolution spectra. However, the current SRPM NLTE approximations are not exact and produce incorrect line cores that have important effects in the UV flux. Currently we are working on using SRPM full NLTE computations similar to those now used for  $H$ , as necessary, for all levels of all species.

This work was supported by NASA contract NAS5-97045 at the University of Colorado. We thank M. Rust and R. Meisner, and the High Altitude Observatory for providing the PSPT data. We acknowledge the referee for his constructive comments that helped improve this paper.

## APPENDIX A

### THE MODELS

In Tables 3–9 we list the model photospheres. The electron densities listed assume LTE for species other than  $H$  and  $H^-$ . We are able to solve the full NLTE equations for all elements, resulting in slightly different electron densities at the top of the listed photospheric models. However, the NLTE values depending on chromospheric layers above that will be addressed in future papers; for this reason we do not consider these NLTE values in this paper.

The turbulent pressure velocities,  $V_{tp}$ , contribute to the density stratification in our models and are not used for computing broadening of the line profiles. The turbulent line-broadening velocity,  $V_{tb}$ , is used as usual to compute line profiles. For the quiet Sun, we compute the line profiles assuming that  $V_{tb} = V_{tp}$ , and this choice does not conflict with observations. However, for active region

TABLE 3  
MODEL C

Gas Pressure (dyne cm <sup>-2</sup> )	Temperature (K)	Height (km)	$N_e$ (cm <sup>-3</sup> )	$N_p$ (cm <sup>-3</sup> )	$N_a$ (cm <sup>-3</sup> )	Turb. Pres. Vel. (km s <sup>-1</sup> )
4.501E+03.....	4.610E+03	4.032E+02	6.847E+11	1.439E+10	6.430E+15	3.945E-01
7.089E+03.....	4.690E+03	3.532E+02	1.009E+12	2.437E+10	9.954E+15	3.396E-01
1.107E+04.....	4.780E+03	3.032E+02	1.498E+12	4.356E+10	1.524E+16	3.581E-01
1.709E+04.....	4.880E+03	2.532E+02	2.237E+12	8.338E+10	2.306E+16	4.812E-01
2.609E+04.....	4.990E+03	2.032E+02	3.357E+12	1.727E+11	3.442E+16	6.717E-01
3.210E+04.....	5.060E+03	1.782E+02	4.141E+12	2.688E+11	4.177E+16	7.352E-01
3.927E+04.....	5.150E+03	1.532E+02	5.154E+12	4.586E+11	5.021E+16	8.786E-01
4.784E+04.....	5.270E+03	1.282E+02	6.567E+12	8.827E+11	5.978E+16	9.922E-01
5.791E+04.....	5.410E+03	1.032E+02	8.611E+12	1.777E+12	7.049E+16	1.130E+00
6.968E+04.....	5.580E+03	7.816E+01	1.192E+13	3.768E+12	8.222E+16	1.258E+00
8.316E+04.....	5.790E+03	5.316E+01	1.797E+13	8.365E+12	9.456E+16	1.414E+00
9.216E+04.....	5.980E+03	3.816E+01	2.588E+13	1.533E+13	1.015E+17	1.493E+00
1.018E+05.....	6.180E+03	2.316E+01	3.857E+13	2.701E+13	1.084E+17	1.572E+00
1.085E+05.....	6.340E+03	1.316E+01	5.279E+13	4.052E+13	1.126E+17	1.628E+00
1.156E+05.....	6.520E+03	3.159E+00	7.457E+13	6.153E+13	1.166E+17	1.672E+00
1.229E+05.....	6.720E+03	-6.841E+00	1.081E+14	9.420E+13	1.202E+17	1.709E+00
1.303E+05.....	6.980E+03	-1.684E+01	1.700E+14	1.552E+14	1.227E+17	1.756E+00
1.380E+05.....	7.280E+03	-2.684E+01	2.770E+14	2.610E+14	1.244E+17	1.792E+00
1.457E+05.....	7.590E+03	-3.684E+01	4.429E+14	4.255E+14	1.256E+17	1.859E+00
1.536E+05.....	7.900E+03	-4.684E+01	6.853E+14	6.664E+14	1.267E+17	1.888E+00
1.615E+05.....	8.220E+03	-5.684E+01	1.040E+15	1.019E+15	1.274E+17	1.940E+00
1.693E+05.....	8.540E+03	-6.684E+01	1.531E+15	1.509E+15	1.277E+17	2.000E+00
1.776E+05.....	8.860E+03	-7.684E+01	2.195E+15	2.170E+15	1.279E+17	2.000E+00
1.859E+05.....	9.140E+03	-8.684E+01	2.954E+15	2.927E+15	1.284E+17	2.000E+00
1.944E+05.....	9.400E+03	-9.684E+01	3.834E+15	3.805E+15	1.289E+17	2.000E+00

NOTE.—Table 3 is also available in machine-readable form in the electronic edition of the *Astrophysical Journal*.

TABLE 4  
MODEL E

Gas Pressure (dyne cm <sup>-2</sup> )	Temperature (K)	Height (km)	$N_e$ (cm <sup>-3</sup> )	$N_p$ (cm <sup>-3</sup> )	$N_a$ (cm <sup>-3</sup> )	Turb. Pres. Vel. (km s <sup>-1</sup> )
4.532E+03 .....	4.647E+03	4.037E+02	7.350E+11	1.998E+10	6.422E+15	3.927E-01
7.115E+03 .....	4.717E+03	3.537E+02	1.073E+12	3.179E+10	9.933E+15	3.397E-01
1.109E+04 .....	4.791E+03	3.037E+02	1.583E+12	5.158E+10	1.524E+16	3.584E-01
1.711E+04 .....	4.880E+03	2.537E+02	2.348E+12	9.054E+10	2.309E+16	4.812E-01
2.612E+04 .....	4.990E+03	2.037E+02	3.504E+12	1.801E+11	3.447E+16	6.694E-01
3.214E+04 .....	5.060E+03	1.787E+02	4.306E+12	2.749E+11	4.183E+16	7.337E-01
3.933E+04 .....	5.150E+03	1.537E+02	5.333E+12	4.618E+11	5.028E+16	8.763E-01
4.791E+04 .....	5.270E+03	1.287E+02	6.747E+12	8.804E+11	5.986E+16	9.931E-01
5.799E+04 .....	5.410E+03	1.037E+02	8.780E+12	1.766E+12	7.058E+16	1.131E+00
6.977E+04 .....	5.580E+03	7.872E+01	1.206E+13	3.747E+12	8.233E+16	1.258E+00
8.327E+04 .....	5.790E+03	5.372E+01	1.809E+13	8.336E+12	9.468E+16	1.415E+00
9.227E+04 .....	5.980E+03	3.872E+01	2.598E+13	1.530E+13	1.016E+17	1.497E+00
1.019E+05 .....	6.180E+03	2.372E+01	3.865E+13	2.699E+13	1.085E+17	1.574E+00
1.086E+05 .....	6.340E+03	1.372E+01	5.287E+13	4.051E+13	1.128E+17	1.631E+00
1.157E+05 .....	6.520E+03	3.721E+00	7.466E+13	6.155E+13	1.167E+17	1.674E+00
1.230E+05 .....	6.720E+03	-6.279E+00	1.082E+14	9.425E+13	1.204E+17	1.707E+00
1.305E+05 .....	6.980E+03	-1.628E+01	1.701E+14	1.552E+14	1.228E+17	1.758E+00
1.382E+05 .....	7.280E+03	-2.628E+01	2.772E+14	2.612E+14	1.245E+17	1.795E+00
1.458E+05 .....	7.590E+03	-3.628E+01	4.432E+14	4.258E+14	1.257E+17	1.863E+00
1.538E+05 .....	7.900E+03	-4.628E+01	6.858E+14	6.669E+14	1.269E+17	1.889E+00
1.616E+05 .....	8.220E+03	-5.628E+01	1.041E+15	1.020E+15	1.275E+17	1.951E+00
1.695E+05 .....	8.540E+03	-6.628E+01	1.532E+15	1.510E+15	1.278E+17	2.000E+00
1.778E+05 .....	8.860E+03	-7.628E+01	2.196E+15	2.172E+15	1.280E+17	2.000E+00
1.862E+05 .....	9.140E+03	-8.628E+01	2.956E+15	2.929E+15	1.285E+17	2.000E+00
1.946E+05 .....	9.400E+03	-9.628E+01	3.837E+15	3.808E+15	1.290E+17	2.000E+00

NOTE.—Table 4 is also available in machine-readable form in the electronic edition of the *Astrophysical Journal*.

TABLE 5  
MODEL F

Gas Pressure (dyne cm <sup>-2</sup> )	Temperature (K)	Height (km)	$N_e$ (cm <sup>-3</sup> )	$N_p$ (cm <sup>-3</sup> )	$N_a$ (cm <sup>-3</sup> )	Turb. Pres. Vel. (km s <sup>-1</sup> )
4.597E+03 .....	4.688E+03	4.042E+02	7.476E+11	2.843E+10	6.458E+15	3.898E-01
7.191E+03 .....	4.752E+03	3.542E+02	1.096E+12	4.335E+10	9.965E+15	3.399E-01
1.117E+04 .....	4.831E+03	3.042E+02	1.616E+12	7.103E+10	1.522E+16	3.590E-01
1.718E+04 .....	4.910E+03	2.542E+02	2.390E+12	1.156E+11	2.304E+16	4.838E-01
2.616E+04 .....	5.018E+03	2.042E+02	3.556E+12	2.188E+11	3.433E+16	6.689E-01
3.217E+04 .....	5.060E+03	1.792E+02	4.324E+12	2.845E+11	4.187E+16	7.320E-01
3.937E+04 .....	5.150E+03	1.542E+02	5.347E+12	4.694E+11	5.034E+16	8.690E-01
4.796E+04 .....	5.270E+03	1.292E+02	6.757E+12	8.844E+11	5.993E+16	9.873E-01
5.805E+04 .....	5.410E+03	1.042E+02	8.787E+12	1.766E+12	7.065E+16	1.128E+00
6.984E+04 .....	5.580E+03	7.923E+01	1.207E+13	3.744E+12	8.241E+16	1.260E+00
8.335E+04 .....	5.790E+03	5.423E+01	1.810E+13	8.335E+12	9.477E+16	1.416E+00
9.236E+04 .....	5.980E+03	3.923E+01	2.599E+13	1.530E+13	1.017E+17	1.498E+00
1.020E+05 .....	6.180E+03	2.423E+01	3.867E+13	2.700E+13	1.086E+17	1.576E+00
1.087E+05 .....	6.340E+03	1.423E+01	5.289E+13	4.053E+13	1.129E+17	1.632E+00
1.158E+05 .....	6.520E+03	4.231E+00	7.469E+13	6.158E+13	1.168E+17	1.674E+00
1.231E+05 .....	6.720E+03	-5.769E+00	1.082E+14	9.429E+13	1.205E+17	1.709E+00
1.306E+05 .....	6.980E+03	-1.577E+01	1.702E+14	1.553E+14	1.229E+17	1.760E+00
1.383E+05 .....	7.280E+03	-2.577E+01	2.774E+14	2.613E+14	1.246E+17	1.797E+00
1.460E+05 .....	7.590E+03	-3.577E+01	4.434E+14	4.260E+14	1.258E+17	1.865E+00
1.539E+05 .....	7.900E+03	-4.577E+01	6.861E+14	6.672E+14	1.270E+17	1.892E+00
1.617E+05 .....	8.220E+03	-5.577E+01	1.041E+15	1.020E+15	1.276E+17	1.959E+00
1.697E+05 .....	8.540E+03	-6.577E+01	1.533E+15	1.510E+15	1.280E+17	2.000E+00
1.780E+05 .....	8.860E+03	-7.577E+01	2.197E+15	2.173E+15	1.281E+17	2.000E+00
1.864E+05 .....	9.140E+03	-8.577E+01	2.957E+15	2.930E+15	1.287E+17	2.000E+00
1.948E+05 .....	9.400E+03	-9.577E+01	3.839E+15	3.810E+15	1.292E+17	2.000E+00

NOTE.—Table 5 is also available in machine-readable form in the electronic edition of the *Astrophysical Journal*.

TABLE 6  
MODEL H

Gas Pressure (dyne cm <sup>-2</sup> )	Temperature (K)	Height (km)	$N_e$ (cm <sup>-3</sup> )	$N_p$ (cm <sup>-3</sup> )	$N_a$ (cm <sup>-3</sup> )	Turb. Pres. Vel. (km s <sup>-1</sup> )
4.670E+03.....	4.781E+03	4.061E+02	6.802E+11	5.801E+10	6.432E+15	5.501E-01
7.391E+03.....	4.832E+03	3.537E+02	1.037E+12	7.679E+10	1.007E+16	5.200E-01
1.135E+04.....	4.897E+03	3.041E+02	1.551E+12	1.092E+11	1.527E+16	5.466E-01
1.718E+04.....	4.970E+03	2.553E+02	2.298E+12	1.635E+11	2.277E+16	6.206E-01
2.556E+04.....	5.072E+03	2.074E+02	3.405E+12	2.875E+11	3.319E+16	7.612E-01
3.185E+04.....	5.130E+03	1.803E+02	4.243E+12	4.002E+11	4.088E+16	8.652E-01
3.842E+04.....	5.196E+03	1.569E+02	5.176E+12	5.766E+11	4.869E+16	9.580E-01
4.737E+04.....	5.306E+03	1.301E+02	6.656E+12	1.026E+12	5.879E+16	1.061E+00
5.720E+04.....	5.410E+03	1.055E+02	8.479E+12	1.739E+12	6.961E+16	1.157E+00
6.929E+04.....	5.580E+03	7.965E+01	1.178E+13	3.697E+12	8.176E+16	1.257E+00
8.223E+04.....	5.790E+03	5.575E+01	1.770E+13	8.227E+12	9.350E+16	1.353E+00
9.201E+04.....	5.980E+03	3.953E+01	2.571E+13	1.522E+13	1.013E+17	1.414E+00
1.021E+05.....	6.180E+03	2.401E+01	3.849E+13	2.696E+13	1.087E+17	1.473E+00
1.085E+05.....	6.340E+03	1.456E+01	5.262E+13	4.042E+13	1.127E+17	1.510E+00
1.158E+05.....	6.520E+03	4.268E+00	7.451E+13	6.152E+13	1.169E+17	1.551E+00
1.231E+05.....	6.720E+03	-5.636E+00	1.080E+14	9.421E+13	1.204E+17	1.593E+00
1.307E+05.....	6.980E+03	-1.568E+01	1.701E+14	1.553E+14	1.230E+17	1.639E+00
1.385E+05.....	7.280E+03	-2.588E+01	2.774E+14	2.614E+14	1.248E+17	1.682E+00
1.462E+05.....	7.590E+03	-3.578E+01	4.437E+14	4.263E+14	1.261E+17	1.728E+00
1.541E+05.....	7.900E+03	-4.583E+01	6.864E+14	6.675E+14	1.272E+17	1.785E+00
1.621E+05.....	8.220E+03	-5.587E+01	1.042E+15	1.021E+15	1.279E+17	1.821E+00
1.698E+05.....	8.540E+03	-6.519E+01	1.533E+15	1.511E+15	1.280E+17	1.830E+00
1.780E+05.....	8.860E+03	-7.509E+01	2.197E+15	2.173E+15	1.282E+17	1.830E+00
1.876E+05.....	9.140E+03	-8.647E+01	2.967E+15	2.940E+15	1.295E+17	1.830E+00
1.957E+05.....	9.400E+03	-9.604E+01	3.848E+15	3.819E+15	1.298E+17	1.830E+00

NOTE.—Table 6 is also available in machine-readable form in the electronic edition of the *Astrophysical Journal*.

TABLE 7  
MODEL P

Gas Pressure (dyne cm <sup>-2</sup> )	Temperature (K)	Height (km)	$N_e$ (cm <sup>-3</sup> )	$N_p$ (cm <sup>-3</sup> )	$N_a$ (cm <sup>-3</sup> )	Turb. Pres. Vel. (km s <sup>-1</sup> )
4.741E+03.....	4.940E+03	4.158E+02	8.202E+11	1.328E+11	6.319E+15	5.520E-01
7.243E+03.....	5.000E+03	3.658E+02	1.203E+12	1.881E+11	9.539E+15	5.202E-01
1.100E+04.....	5.070E+03	3.158E+02	1.768E+12	2.774E+11	1.428E+16	5.416E-01
1.658E+04.....	5.144E+03	2.658E+02	2.597E+12	4.157E+11	2.123E+16	6.111E-01
2.479E+04.....	5.227E+03	2.158E+02	3.822E+12	6.513E+11	3.123E+16	7.487E-01
3.020E+04.....	5.275E+03	1.908E+02	4.651E+12	8.403E+11	3.770E+16	8.397E-01
3.668E+04.....	5.341E+03	1.658E+02	5.744E+12	1.177E+12	4.522E+16	9.358E-01
4.440E+04.....	5.446E+03	1.408E+02	7.367E+12	1.917E+12	5.368E+16	1.027E+00
5.352E+04.....	5.544E+03	1.158E+02	9.468E+12	2.987E+12	6.357E+16	1.119E+00
6.424E+04.....	5.660E+03	9.079E+01	1.255E+13	4.878E+12	7.473E+16	1.212E+00
7.677E+04.....	5.794E+03	6.579E+01	1.722E+13	8.186E+12	8.722E+16	1.305E+00
8.520E+04.....	5.922E+03	5.079E+01	2.246E+13	1.254E+13	9.472E+16	1.363E+00
9.432E+04.....	6.081E+03	3.579E+01	3.115E+13	2.029E+13	1.021E+17	1.420E+00
1.008E+05.....	6.192E+03	2.579E+01	3.922E+13	2.768E+13	1.071E+17	1.459E+00
1.075E+05.....	6.326E+03	1.579E+01	5.127E+13	3.903E+13	1.119E+17	1.500E+00
1.146E+05.....	6.482E+03	5.793E+00	6.954E+13	5.656E+13	1.163E+17	1.540E+00
1.219E+05.....	6.663E+03	-4.207E+00	9.775E+13	8.396E+13	1.203E+17	1.584E+00
1.294E+05.....	6.855E+03	-1.421E+01	1.386E+14	1.239E+14	1.240E+17	1.638E+00
1.370E+05.....	7.096E+03	-2.421E+01	2.090E+14	1.934E+14	1.268E+17	1.698E+00
1.448E+05.....	7.358E+03	-3.421E+01	3.185E+14	3.016E+14	1.290E+17	1.768E+00
1.528E+05.....	7.621E+03	-4.421E+01	4.732E+14	4.550E+14	1.311E+17	1.825E+00
1.612E+05.....	7.862E+03	-5.421E+01	6.694E+14	6.498E+14	1.337E+17	1.830E+00
1.698E+05.....	8.127E+03	-6.421E+01	9.556E+14	9.343E+14	1.358E+17	1.830E+00
1.786E+05.....	8.378E+03	-7.421E+01	1.313E+15	1.290E+15	1.379E+17	1.830E+00
1.875E+05.....	8.623E+03	-8.421E+01	1.764E+15	1.739E+15	1.398E+17	1.830E+00

NOTE.—Table 7 is also available in machine-readable form in the electronic edition of the *Astrophysical Journal*.



TABLE 8  
MODEL R

Gas Pressure (dyne cm <sup>-2</sup> )	Temperature (K)	Height (km)	$N_e$ (cm <sup>-3</sup> )	$N_p$ (cm <sup>-3</sup> )	$N_a$ (cm <sup>-3</sup> )	Turb. Pres. Vel. (km s <sup>-1</sup> )
4.120E+03.....	4.590E+03	4.198E+02	6.961E+11	1.385E+10	5.910E+15	4.200E-01
5.327E+03.....	4.622E+03	3.917E+02	8.563E+11	1.759E+10	7.590E+15	3.800E-01
6.875E+03.....	4.658E+03	3.637E+02	1.056E+12	2.285E+10	9.718E+15	3.600E-01
8.853E+03.....	4.701E+03	3.357E+02	1.306E+12	3.055E+10	1.240E+16	3.600E-01
1.138E+04.....	4.727E+03	3.075E+02	1.623E+12	3.671E+10	1.586E+16	3.621E-01
1.462E+04.....	4.759E+03	2.794E+02	2.018E+12	4.543E+10	2.023E+16	3.789E-01
1.876E+04.....	4.801E+03	2.511E+02	2.513E+12	5.945E+10	2.573E+16	4.127E-01
2.404E+04.....	4.856E+03	2.226E+02	3.142E+12	8.276E+10	3.261E+16	4.639E-01
3.080E+04.....	4.927E+03	1.937E+02	3.957E+12	1.257E+11	4.117E+16	5.333E-01
3.382E+04.....	4.951E+03	1.826E+02	4.320E+12	1.457E+11	4.498E+16	5.869E-01
3.843E+04.....	4.972E+03	1.674E+02	4.858E+12	1.672E+11	5.089E+16	6.351E-01
4.373E+04.....	4.991E+03	1.519E+02	5.470E+12	1.915E+11	5.769E+16	6.892E-01
4.986E+04.....	5.044E+03	1.361E+02	6.237E+12	2.609E+11	6.509E+16	7.498E-01
5.696E+04.....	5.115E+03	1.197E+02	7.189E+12	3.924E+11	7.333E+16	8.176E-01
6.523E+04.....	5.218E+03	1.028E+02	8.456E+12	6.898E+11	8.231E+16	8.940E-01
7.489E+04.....	5.356E+03	8.504E+01	1.028E+13	1.395E+12	9.208E+16	9.802E-01
8.621E+04.....	5.517E+03	6.635E+01	1.313E+13	2.974E+12	1.029E+17	1.078E+00
9.675E+04.....	5.637E+03	5.056E+01	1.630E+13	5.000E+12	1.130E+17	1.166E+00
1.031E+05.....	5.740E+03	4.160E+01	1.938E+13	7.412E+12	1.183E+17	1.219E+00
1.109E+05.....	5.826E+03	3.125E+01	2.299E+13	1.021E+13	1.253E+17	1.282E+00
1.185E+05.....	5.939E+03	2.163E+01	2.841E+13	1.486E+13	1.313E+17	1.342E+00
1.272E+05.....	6.101E+03	1.099E+01	3.844E+13	2.404E+13	1.372E+17	1.411E+00
1.369E+05.....	6.290E+03	-3.555E-01	5.519E+13	3.982E+13	1.432E+17	1.487E+00
1.473E+05.....	6.452E+03	-1.201E+01	7.585E+13	5.943E+13	1.502E+17	1.568E+00
1.580E+05.....	6.630E+03	-2.362E+01	1.063E+14	8.881E+13	1.568E+17	1.651E+00
1.690E+05.....	6.809E+03	-3.508E+01	1.480E+14	1.293E+14	1.632E+17	1.736E+00
1.801E+05.....	7.015E+03	-4.622E+01	2.124E+14	1.924E+14	1.687E+17	1.821E+00
1.912E+05.....	7.223E+03	-5.707E+01	3.013E+14	2.800E+14	1.738E+17	1.907E+00
2.023E+05.....	7.443E+03	-6.763E+01	4.268E+14	4.039E+14	1.782E+17	1.992E+00
2.133E+05.....	7.682E+03	-7.795E+01	6.097E+14	5.852E+14	1.817E+17	2.078E+00
2.244E+05.....	7.980E+03	-8.814E+01	9.192E+14	8.927E+14	1.835E+17	2.165E+00
2.355E+05.....	8.215E+03	-9.829E+01	1.252E+15	1.223E+15	1.864E+17	2.254E+00
2.560E+05.....	8.616E+03	-1.165E+02	2.050E+15	2.018E+15	1.918E+17	2.393E+00
2.677E+05.....	8.845E+03	-1.269E+02	2.663E+15	2.628E+15	1.943E+17	2.490E+00

NOTE.—Table 8 is also available in machine-readable form in the electronic edition of the *Astrophysical Journal*.

TABLE 9  
MODEL S

Gas Pressure (dyne cm <sup>-2</sup> )	Temperature (K)	Height (km)	$N_e$ (cm <sup>-3</sup> )	$N_p$ (cm <sup>-3</sup> )	$N_a$ (cm <sup>-3</sup> )	Turb. Pres. Vel. (km s <sup>-1</sup> )	BHminus
2.285E+03.....	3.593E+03	4.278E+02	6.999E+10	1.158E+06	4.189E+15	8.800E-01	1.059E+00
5.590E+03.....	3.587E+03	3.501E+02	1.276E+11	1.798E+06	1.026E+16	9.772E-01	1.024E+00
1.399E+04.....	3.600E+03	2.698E+02	2.518E+11	3.263E+06	2.559E+16	1.096E+00	1.009E+00
3.160E+04.....	3.611E+03	1.978E+02	4.592E+11	5.520E+06	5.764E+16	1.228E+00	1.003E+00
6.480E+04.....	3.642E+03	1.333E+02	8.089E+11	1.032E+07	1.172E+17	1.362E+00	1.001E+00
1.151E+05.....	3.692E+03	8.099E+01	1.327E+12	2.131E+07	2.054E+17	1.451E+00	1.000E+00
1.719E+05.....	3.772E+03	4.330E+01	2.028E+12	5.351E+07	3.001E+17	1.580E+00	9.999E-01
2.226E+05.....	3.896E+03	1.798E+01	3.040E+12	1.765E+08	3.763E+17	1.709E+00	9.999E-01
2.652E+05.....	4.040E+03	6.451E-01	4.444E+12	6.122E+08	4.324E+17	1.731E+00	9.999E-01
2.921E+05.....	4.170E+03	-9.587E+00	5.895E+12	1.707E+09	4.613E+17	1.809E+00	9.999E-01
3.208E+05.....	4.320E+03	-1.968E+01	7.848E+12	5.319E+09	4.890E+17	1.858E+00	9.999E-01
3.513E+05.....	4.490E+03	-2.958E+01	1.046E+13	1.808E+10	5.152E+17	1.873E+00	9.999E-01
3.799E+05.....	4.680E+03	-3.871E+01	1.392E+13	6.394E+10	5.345E+17	1.931E+00	9.999E-01
4.096E+05.....	4.890E+03	-4.796E+01	1.851E+13	2.312E+11	5.516E+17	2.000E+00	9.999E-01
4.442E+05.....	5.120E+03	-5.826E+01	2.446E+13	8.431E+11	5.713E+17	2.060E+00	9.999E-01
4.801E+05.....	5.360E+03	-6.888E+01	3.194E+13	2.859E+12	5.898E+17	2.156E+00	1.000E+00
5.255E+05.....	5.620E+03	-8.143E+01	4.375E+13	9.179E+12	6.157E+17	2.212E+00	1.000E+00
5.685E+05.....	5.870E+03	-9.311E+01	6.240E+13	2.356E+13	6.378E+17	2.292E+00	1.000E+00
6.222E+05.....	6.140E+03	-1.072E+02	9.797E+13	5.487E+13	6.672E+17	2.386E+00	1.000E+00
6.689E+05.....	6.420E+03	-1.184E+02	1.599E+14	1.133E+14	6.859E+17	2.404E+00	1.000E+00
7.122E+05.....	6.700E+03	-1.284E+02	2.609E+14	2.111E+14	6.996E+17	2.419E+00	1.000E+00
7.564E+05.....	7.000E+03	-1.385E+02	4.324E+14	3.790E+14	7.108E+17	2.434E+00	1.000E+00

NOTE.—Table 9 is also available in machine-readable form in the electronic edition of the *Astrophysical Journal*.

models (H, P, R, S) the line-broadening velocities should be determined from spectral line observations that are beyond the scope of this paper. For line broadening in active region models we recommend using values such that  $V_{tb} < V_{tp}$  and also to take into account the Zeeman splitting.

The NLTE departure coefficients for  $H^-$  are listed here for the sunspot model only. For the other models these coefficients are unity over the range of these tables.

## APPENDIX B

### THE ANNULI MEDIAN AND THE CLV

The average of a function within an annulus should be considered using the weight given by the area at each value of  $\mu$ . Thus, this average is given by the following equation,

$$\langle f \rangle = \frac{\int_{\mu_b}^{\mu_a} f r dr}{\int_{\mu_b}^{\mu_a} r dr} = \frac{\int_{\mu_b}^{\mu_a} f \mu d\mu}{\int_{\mu_b}^{\mu_a} \mu d\mu} = \frac{2 \int_{\mu_b}^{\mu_a} f \mu d\mu}{(\mu_b^2 - \mu_a^2)}, \quad (B1)$$

where  $\langle f \rangle$  is the average value of the function in the interval of  $\mu$  between  $\mu_a$  and  $\mu_b$  and  $r$  is the relative radius.

Using this formula we derive the center-of-gravity value of  $\mu$  in an annulus

$$\langle \mu \rangle = \frac{2(\mu_b^3 - \mu_a^3)}{3(\mu_b^2 - \mu_a^2)} \text{ and } \langle \mu^2 \rangle = \frac{(\mu_b^2 + \mu_a^2)}{2}. \quad (B2)$$

For our study of the PSPT CLV we split the solar disk in 10 annuli (or bins in  $\mu$ ) and use this formula within each of them to determine  $\mu$  for the center of gravity of the pixels. Then, we evaluate the median of the pixel intensities in each annulus and assign that value to this  $\mu$ . The reason for using the median to obtain the quiet-Sun limb darkening, instead of the average, is that any solar activity present on the disk can significantly affect the average values because of the large contrast of sunspots. Even when the area of sunspots is relatively small, if one uses too small bins in  $\mu$ , then the average value can be significantly affected. To minimize this issue we use the median for each bin because in using this, each pixel value is weighted by the same amount regardless of its contrast (this is a standard technique for minimizing the effects of “outliers” in the fitting process).

A fit to a Legendre polynomial can be used to approximate the CLV curves for the observations; using a fixed degree of this polynomial, it is possible to perform simple comparisons between various types of observations. Considering a second-order Legendre polynomial that passes through three points, namely,  $a$ ,  $b$ , and  $c$ , it is not difficult to find analytical expressions for the coefficient of the polynomial given as follows,

$$f(\mu) = F_0 + F_1\mu + F_2(\mu^2 - 1), \quad (B3)$$

and the coefficients are

$$F_2 = \frac{(\mu_b - \mu_c)(f_a - f_b) - (\mu_a - \mu_b)(f_b - f_c)}{(\mu_b - \mu_c)(\mu_a^2 - \mu_b^2) - (\mu_a - \mu_b)(\mu_b^2 - \mu_c^2)}, \quad (B4)$$

$$F_1 = \frac{(f_a - f_b) - F_2(\mu_a^2 - \mu_b^2)}{(\mu_a - \mu_b)}, \quad (B5)$$

$$F_0 = f_a - F_1\mu_a - F_2(\mu_a^2 - 1). \quad (B6)$$

If we consider the weighted average of this polynomial over an interval of  $\mu$ , it is

$$\langle f(\mu) \rangle = F_0 + F_1\langle \mu \rangle + F_2(\langle \mu^2 \rangle - 1), \quad (B7)$$

and if we now consider three intervals of  $\mu$  and the corresponding averages of  $f$ , one can solve for the coefficients as before and obtain similar formulas, but where the values of  $\mu$  and its square correspond to the average  $\mu$  and average  $\mu^2$  as shown above. In this case, of course,  $\langle \mu^2 \rangle$  is different from  $\langle \mu \rangle^2$ .

However, as before, it is best to use the median instead of the average, and when using the median in the bins, the medians of  $\mu$  and  $\mu^2$  should be used.

## REFERENCES

- Allende Prieto, C., Lambert, D. L., & Asplund, M. 2002, *ApJ*, 573, L137  
 Aschwanden, M. J., Nightingale, R. W., Tarbell, T. D., & Wolfson, C. J. 2000, *ApJ*, 535, 1027  
 Asplund, M., Grevesse, N., & Sauval, A. J. 2004a, in *ASP Conf. Ser.* 336, *Cosmic Abundances as Records of Stellar Evolution and Nucleosynthesis*, ed. F. N. Bash & T. G. Barnes III (San Francisco: ASP), 25  
 Asplund, M., Grevesse, N., Sauval, A. J., Allende Prieto, C., & Kiselman, D. 2004b, *A&A*, 417, 751  
 Avrett, E. H. 1985, in *Chromospheric Diagnostics and Modeling*, ed. B. W. Lites (Sunspot: NSO), 67  
 Avrett, E. H., & Loeser, R. 2003, in *IAU Symp.* 210, *Modelling of Stellar Atmospheres* (San Francisco: ASP), A21  
 Ayres, T. R., & Rabin, D. 1996, *ApJ*, 460, 1042  
 Balthasar, H., & Collados, M. 2005, *A&A*, 429, 705  
 Berger, T. E., et al. 2004, *A&A*, 428, 613  
 Carlsson, M., & Stein, R. F. 1997, *ApJ*, 481, 500  
 Chapman, G. A. 1977, *ApJS*, 33, 35  
 Cowley, C. R., & Bautista, M. 2003, *MNRAS*, 341, 1226  
 Curdt, W., Brekke, P., Feldman, U., Wilhelm, K., Dwivedi, B. N., Schühle, U., & Lemaire, P. 2001, *A&A*, 375, 591

- del Toro Iniesta, J. C., Tarbell, T. D., & Ruiz Cobo, B. 1994, *ApJ*, 436, 400
- Ding, M. D., & Fang, C. 1989, *A&A*, 225, 204
- Ding, M. D., & Schleicher, H. 1998, *A&A*, 332, 767
- Dodson, H. W. 1954, *ApJ*, 119, 564
- Ellison, M. A. 1952, *MNRAS*, 112, 679
- Falconer, D. A., Gary, G. A., Moore, R. L., & Porter, J. G. 2000, *ApJ*, 528, 1004
- Fontenla, J. M. 2005, *A&A*, 442, 1099
- Fontenla, J. M., Avrett, E., & Loeser, R. 1990, *ApJ*, 355, 700 (FAL90)
- . 1991, *ApJ*, 377, 712 (FAL91)
- . 1993, *ApJ*, 406, 319 (FAL93)
- . 2002, *ApJ*, 572, 636 (FAL02)
- Fontenla, J. M., Harder, J., Rottman, G., Woods, T. N., Lawrence, G. M., & Davis, S. 2004, *ApJ*, 605, L85
- Fontenla, J., Reichmann, E. J., & Tandberg-Hanssen, E. 1988, *ApJ*, 329, 464
- Fontenla, J., White, O. R., Fox, P. A., Avrett, E. H., & Kurucz, R. L. 1999, *ApJ*, 518, 480
- Gingerich, O., & de Jager, C. 1968, *Sol. Phys.*, 3, 5
- Gingerich, O., Noyes, R. W., Kalkofen, W., & Cuny, Y. 1971, *Sol. Phys.*, 18, 347
- Gray, R. O., & Corbally, C. J. 1994, *AJ*, 107, 742
- Grevesse, N., & Sauval, A. J. 2000, in *Origin of Elements in the Solar System, Implications of Post-1957 Observations*, ed. O. Manuel (Dordrecht: Kluwer), 261
- Harder, J., Lawrence, G. M., Fontenla, J. M., Rottman, G., & Woods, T. N. 2005, *Sol. Phys.*, 230, 141
- Judge, P., Carlsson, M., & Wilhelm, K. 1997, *ApJ*, 490, L195
- Kalkofen, W. 2001, *ApJ*, 557, 376
- Keller, C. U., Schüssler, M., Vögler, A., & Zakharov, V. 2004, *ApJ*, 607, L59
- Kjeldseth-Moe, O., & Maltby, P. 1969, *Sol. Phys.*, 8, 275
- . 1974, *Sol. Phys.*, 36, 101
- Kneer, F., & von Uexkull, M. 1986, *A&A*, 155, 178
- Kurucz, R. L. 1992a, in *IAU Symp. 149, The Stellar Populations of Galaxies*, ed. B. Barbara & A. Renzini (Dordrecht: Kluwer), 225
- . 1992b, *Rev. Mex. AA*, 23, 181
- Kurucz, R. L., van Dishoeck, E. F., & Tarafdar, S. P. 1987, *ApJ*, 322, 992
- Lemaire, P., Gouttebroze, P., Vial, J. C., & Artzener, G. E. 1981, *A&A*, 103, 160
- Lites, B. W., & Skumanich, A. 1982, *ApJS*, 49, 293
- Malherbe, J.-M., Roudier, T., Mein, P., Moity, J., & Muller, R. 2004, *A&A*, 427, 745
- Maltby, P., Avrett, E. H., Carlsson, M., Kjeldset-Moe, O., Kurucz, R., & Loeser, R. 1986, *ApJ*, 306, 284
- Mandel, H., Labs, D., Thuillier, G., Herse, M., Simon, P. C., & Gillotay, D. 1998, *Metrologia*, 35, 697
- Melendez, J. 2004, *ApJ*, 615, 1042
- Morrill, J. S., Dere, K. P., & Korendyke, C. M. 2001, *ApJ*, 557, 854
- Neckel, H., & Labs, D. 1984, *Sol. Phys.*, 90, 205
- . 1994, *Sol. Phys.*, 153, 91
- Penza, V., Caccin, B., Ermolli, I., & Centrone, M. 2004, *A&A*, 413, 1115
- Pierce, A. K. 1954, *Sol. Phys.*, 119, 312
- . 2000, in *Allen's Astrophysical Quantities*, ed. A. N. Cox (New York: Springer), 355
- Pierce, A. K., & Slaughter, C. D. 1977, *Sol. Phys.*, 51, 25
- Pierce, A. K., Slaughter, C. D., & Weinberger, W. 1977, *Sol. Phys.*, 52, 179
- Sanchez Cuberes, M., Vazquez, M., Bonet, J. A., & Sobotka, M. 2002, *ApJ*, 570, 886
- Schrijver, C. J., Coté, J., Zwaan, C., & Saar, S. H. 1989, *ApJ*, 337, 964
- Secchi, A. 1865, *Astron. Register*, 3, 275
- Solanki, S. 2000, in *Allen's Astrophysical Quantities*, ed. A. N. Cox (New York: Springer), 367
- Spruit, H. C. 1976, *Sol. Phys.*, 50, 269
- Tarafdar, S. P., & Vardya, M. S. 1972, *ApJ*, 171, 185
- Thuillier, G., Herse, M., Labs, D., Foujols, T., Peetermans, W., Gillotay, D., Simon, P. C., & Mandel, H. 2003, *Sol. Phys.*, 214, 1
- Vernazza, J. E., Avrett, E., & Loeser, R. 1981, *ApJS*, 45, 635 (VAL81)
- Vogler, F. L., Brandt, P. N., Otruba, W., & Hanslmeier, A. 2005, in *Solar Magnetic Phenomena*, ed. A. Hanslmeier, A. Veronig, & M. Messerotti (Dordrecht: Springer), 191
- von Uexkull, M., & Kneer, F. 1995, *A&A*, 294, 252
- Wallace, L., Hinkle, K., & Livingston, W. 1998, *An Atlas of the Spectrum of the Solar Photosphere from 13,500 to 28,000 cm<sup>-1</sup> (3570–7405 Å)* (NSO Tech. Rep. 98-001; Tucson: NSO)
- Walton, S. R. 1987, *ApJ*, 312, 909
- Weck, P. F., Schweitzer, A., Stancil, P. C., Hauschildt, P. H., & Kirby, K. 2003, *ApJ*, 584, 459
- Wikstøl, Ø., Hansteen, V. H., Carlsson, M., & Judge, P. G. 2000, *ApJ*, 531, 1150